Check for updates

Energy Technology
Generation, Conversion, Storage, Distribution
www.entechnol.de

Solar Array Optimization Using Cryptographic Fibonacci Transformation for Global Power Enhancement and Ease of MPPT Controllers

Rayappa David Amar Raj and Kanasottu Anil Naik*

The photovoltaic array reconfiguration approach is the most promising solution to enhance the global maximum power (GMP) and improve the array characteristics by mitigating the variation between distinct rows, thereby reducing the computational burden on maximum power point tracking systems. However, the majority of the existing reconfiguration approaches inherently have many drawbacks such as scalability issues, poor shade dispersion, distorted array characteristics, numerous power peaks, augmented mismatch, etc. In order to address these issues, this article proposes a novel integer-based Fibonacci transform technique using the idea of image encryption for reconfiguration. The proposed strategy is tested for both symmetric and asymmetric photovoltaic (PV) arrays under 19 shading cases. Further, its performance is compared with the 23 existing techniques. Besides, a nonparametric Wilcoxon signed-rank sum test with a significant difference (p-value) of 0.05 is used to perform a pairwise unbiased comparison of all the techniques. Due to the discriminate shade dispersion through intelligent reconfiguration, the proposed strategy delivers consistently superior performance yielding the respective GMP enhancement of 34.43%, 12.5%, 5.06%, and 37.39%, 22.94%, 16.5% for 9 × 9, and 4 × 8 PV arrays under distinct cases. The proposed algorithm is further validated using the Levenberg–Marquardt neural network-based MPPT controller for a 7 kWp standalone PV system.

1. Introduction

The initiative to increase the use of sources of renewable power has been driven by the demand for pollution-free, green, and clean energy. Photovoltaic (PV) technological advances can aid in the powering of urban and rural regions in tropical countries since they can use solar irradiation throughout the year. Solar power generation is intermittent because of the sun's daily and seasonal variations in insolation.

R. D. A. Raj, K. A. Naik
Department of Electrical Engineering
National Institute of Technology
Warangal 506004, India
E-mail: rd721025@student.nitw.ac.in

The ORCID identification number(s) for the author(s) of this article can be found under https://doi.org/10.1002/ente.202300380.

DOI: 10.1002/ente.202300380

1.1. Motivation and Research Problem

PV panels are subjected to a commonly and regularly occurring phenomenon termed partial shading (PS). The shading of the solar panels alters their electrical characteristics. The discrepancies in the characteristics of the connected panels in an array lead to a mismatch between them, resulting in mismatch losses.[1] Due to PS, the shaded panel acts as a sink absorbing the power, and the unshaded panels act as a source. The huge concentration of currents at the shaded panel instigates the formation of hotspots which may further cause dangerous fire hazards. To avoid these ill effects, bypass protection diodes are to be installed, which bypass the current during PS. However, these diodes provoke numerous peaks in the array characteristics.[2] The existence of these multiple power peaks (MPPs) necessitates a maximum power point tracking (MPPT) controller[3] to operate the array at the global maximum power (GMP). Notwithstanding, the simple and conventional MPPT techniques may struck at the local maximum, offering suboptimal output. Hence, an efficient MPPT controller is required to track the GMP, for which many recent techniques are suggested. A conventional perturb and observed MPPT controller had been employed in ref.[4] for controlling the grid-connected solar system that incorporates the capabilities of an active power filter. An MPPT controller based on an ant colony optimization algorithm that trains the designed ANN is proposed in ref.[5] for improved GMP tracking at a quicker speed, more resilience, and lower steady-state oscillations. Further, the ANFIS-based MPPT algorithm integrated with the particle swarm optimizer[6] is designed for a PV-powered brushless DC electric motor-based wire feeder. However, these controllers, regardless of their sophistication level, cannot extract the full potential of the array and just track its GMP. Further, to enhance the array output even beyond what is obtainable by employing the MPPT alone, array reconfiguration is preferred.

1.2. Literature Review

In general, the reconfiguration strategies are classified as static and dynamic strategies based on their mode of operation.

 © 2023 Wiley-VCH GmbH

The dynamic strategies are further grouped into artificial intelligence (AI), electrical array reconfiguration (EAR), and metaheuristic-based[7–11] strategies. The AI-based techniques[12,13] mitigate the mismatch losses; however, they involve both fixed and adaptive parts of an array in which only the adaptive part can be modified and hence failing to obtain the optimal solution. Moreover, they require numerous switches, sensors, switching matrices, complex control algorithms, driver circuits, etc., making the solution highly cost-ineffective. Besides, the fuzzy methods consume high memory in operating the switching matrix. The EAR-based strategies also employ the aforementioned devices for proper operation and also the implementation of EAR for large-rated PV farms are highly challenging. Further, they generate many switching pulse patterns to find the optimal pattern.

1.3. Research Gaps

Recently, metaheuristic-based algorithms are gaining popularity due to their effectiveness in designing switching matrices for the dynamic reconfiguration of the array. However, all these algorithms suffer major shortcomings such as giant computational steps, time-consuming, convergence issues, numerous parameters, parameters selection difficulties, tuning parameters and weighting factor selection issues, probability of getting stuck at local optimum, large search space, large no. of iterations, complex algorithms, randomness involved, multiple stages to solve, etc. Due to the aforementioned challenges, and practical feasibility issues of dynamic reconfiguration, the static reconfiguration techniques are recommended.

Unlike dynamic strategies, the static techniques do not require sensors, switches, switching matrices, and all other additional equipment for their operation, hence providing an economical solution. Nonetheless, many of the existing static techniques pose numerous drawbacks, as summarized in **Table 1**. It is witnessed from the table that the existing techniques inherit the following shortcomings: scalability issues, indiscriminate shade dispersion, numerous solution sets, increased mismatch in rows, inconsistent performance, and numerous MPPs in the array characteristics imposing a burden on MPPT systems while discriminating the local maximum and global maximum.

1.4. Major Contributions of the Paper

To rectify these drawbacks, a highly efficient integer sequence-based reconfiguration technique named Fibonacci transform (FT) is proposed. The novelty and contributions of the proposed work are as follows: 1) A highly efficient, simple, scalable, sensorless, switchless integer sequence-based PV array reconfiguration approach is proposed to effectively disperse the shade, and its effectiveness is evaluated using image quality indices. 2) As opposed to many static techniques[14–36] that indiscriminately disperse the shade, the proposed technique intelligently disperses the shade. This is achieved by the image scrambling property of the considered integer sequence strategy, where the correlation between the adjacent shaded PV modules in a row, column, and diagonal is highly reduced, thereby improving the total irradiation of a particular row of PV array. 3) Contrary to numerous static reconfiguration techniques, the proposed technique is compatible with all sizes of PV arrays, and it is validated for 9×9, 4×4, and 4×8 PV arrays. 4) The effectiveness of the proposed approach is compared with the recently developed 23 static reconfiguration techniques. 5) The laboratory experimental prototype model of the proposed configuration for a 4×4 PV array has been developed and tested under artificial shading conditions. 6) The proposed algorithm is further validated using the Levenberg-Marquardt neural network-based MPPT controller for a 7 kWp standalone PV system. 7) A pairwise unbiased comparative assessment using a nonparametric Wilcoxon signed rank sum test with a p-value of 0.05 is performed to confirm the consistency and reliability of the proposed technique statistically w.r.t the existing ones.

The organization of the paper is as follows: Section 1 deals with the motivation of paper, literature review, study gaps, and major contributions of the paper. The modeling of PV array is described briefly in Section 2. Section 3 describes the proposed reconfiguration methodology, Levenberg–Marquardt neural network-based MPPT controller and their detailed analysis. Section 4 deals with the results and discussion of the proposed method.

2. Modeling of PV Array

A PV array is typically made up of several series-parallel PV modules, each of which can be built using several series-parallel PV cells. In this work, a commonly used one-diode model[37,38] is provided to describe the generating characteristic of a PV cell, as illustrated in **Figure 1**. The current of the PV cell can be expressed using Kirchhoff's current law as follows

$$I = I_{\mathrm{ph}} - I_{\mathrm{d}} - I_{\mathrm{sh}} \tag{1}$$

where I represent solar cell output current, I_{ph} is the light-generated current, I_{d} and I_{sh} are the currents through the diode and shunt resistance. This equation is made simpler by using I_{o} as the sum of the saturation current and shunt leakage current. As a result, the equation is simplified to

$$I = I_{\mathrm{ph}} - I_{\mathrm{o}} \tag{2}$$

The value of photon current, which is created when a solar cell collects solar radiation and is closely connected with variations in temperature and solar irradiance levels, is given as

$$I_{\mathrm{ph}} = (I_{\mathrm{scr}} + k_i \Delta T)\frac{G}{G_{\mathrm{r}}} \tag{3}$$

where I_{scr} is the rated solar current at nominal climatic conditions 25 °C and 1000 W m^{-2} and k_i represents the short-circuit temperature coefficient. G represents the solar irradiance under typical ambient conditions, and G_r represents the irradiance in W m^{-2}. ΔT is the deviation between the operating temperature (T) and the nominal temperature (T_{ref}). Additionally, the PV cell's reverse saturation current[37,39] will be defined by

$$I_{\mathrm{o}} = I_{\mathrm{rs}}\left(\frac{T}{T_{\mathrm{ref}}}\right)^3 \exp\left(q\frac{E_{\mathrm{go}}}{AK}\right)\left(\frac{\Delta T}{T_{\mathrm{ref}}\, T}\right) \tag{4}$$

© 2023 Wiley-VCH GmbH

21944296, 2023, 9, Downloaded from https://onlinelibrary.wiley.com/doi/10.1002/ente.202300380 by National Institute Of, Wiley Online Library on [27/11/2025]. See the Terms and Conditions (https://onlinelibrary.wiley.com/terms-and-conditions) on Wiley Online Library for rules of use; OA articles are governed by the applicable Creative Commons License

Table 1. Detailed literature survey of various reconfiguration strategies.

Ref	Approach	Category	Array	Description	Drawbacks/limitations
[12]	Neural network (NN)	AI, dynamic	3×4	Employed NN scheme to coordinate the adaptive part of an array to balance row irradiation	Fail to yield an optimal solution, employs numerous switches, sensors, and control units
[7]	Genetic algorithm (GA)	Metaheuristic, dynamic	9×9	Determines the optimal switching matrix pattern using a genetic algorithm	Weighted sum approach, parameter selection issues, may struck at local optimum, convergence issues
[13]	Fuzzy based	AI, dynamic	3×4	Reconfigures the array based on the detection of partial shading	Needs switches, sensors, switching matrix, complex algorithm for detection and reconfiguration
[8]	Particle swarm optimization	Metaheuristic, dynamic	9×9	Determines the optimal switching matrix pattern using particle swarm optimization	Easily trapped in local optimum, tunning parameter challenges, weighted sum approach
[9]	Gray wolf optimization	Metaheuristic, dynamic	9×9	Mitigates row current variation and maximizes the output as a multi-objective problem	Employs weighted sum approach, selecting improper weights affects the optimal solution
[10]	Two-step GA	Metaheuristic, dynamic	9×9	Electrical circuitry is altered via a GA-based two-stage reconfiguration approach	Increased algorithm complexity as it involves two stages of reconfiguration, drawbacks of GA
[11]	Artificial ecosystem	Metaheuristic, dynamic	9×9	Achieves uniform shade dispersion using less parameters	Increased algorithm complexity has parameters with random values resulting in suboptimal output
[47]	Novel dynamic	EAR, dynamic	2×2	Proposes a new dynamic strategy for water pumping system	Practical feasibility on large scale is challenging as it involves the coordination of numerous switches
[14]	Sudoku (SD)	Puzzle-based, static	9×9	Reconfiguration of array based on sudoku puzzle pattern for GMP extraction	Incompatible for asymmetric arrays, exists several solution sets and finding optimal pattern is non-viable
[15]	Futoshiki puzzle (FP)	Puzzle-based, static	9×9	Disperses the shade over the array via FP-based configuration for better array characteristics	Not compatible to asymmetric arrays, inconsistent performance, exists several solution sets
[16]	Shade dispersion (SP)	Magic-square, static	4×4	Reconfigures the array based on magic-square pattern for mismatch mitigation	Ineffective shade dispersion, not compatible to asymmetric arrays
[17]	Latin square (LS)	Puzzle-based, static	4×4	Physical relocation of modules using LS arrangement for TCT configured array	Poor shade dispersion under diagonal shading, incompatible for asymmetric arrays
[18]	Optimal sudoku arrangement (OSA)	Puzzle-based, static	9×9	Achieves better shade dispersion (under many cases) decreasing the MPPs	Scalability issues, similar limitations as that of SD technique, inconsistent performance
[18]	Nonoptimal Sudoku (NOS)	Puzzle-based, static	9×9	Incorporated new rules to the general sudoku puzzle rules to obtain rearranged pattern	Same limitations as that of SD technique, not compatible for asymmetric arrays
[19]	Shift modified (SM)	Shift-based, static	9×9	Performs physical relocation of panels without altering electric circuitry	Failed to demonstrate the effectiveness of algorithm for asymmetric arrays
[20]	Column index (CI)	Index-based, static	9×9	One-time and fixed reconfiguration strategy to disperse the shade	Not tested for asymmetric PV arrays, limited analysis
Ref	Approach	Category	Array	Description	Drawbacks/limitations
[21]	Skyscraper (SC)	Puzzle-based, static	9×9	Reconfiguration based on Skyscraper pattern minimize protection diodes power loss	Fails under diagonal shading, compatibility issues, exists numerous solution sets
[22]	Improved Sudoku (IS)	Puzzle-based, static	9×9	Physical relocation based on improved sudoku pattern for mismatch mitigation	Same limitations as that of SD technique, poor performance under diagonal shading
[23]	Lo Shu (LOS)	Magic-square, static	9×9	Shade dispersion based on the rules of Lo Shu square for improving array characteristics	Compatibility issues, cannot be applicable to other than $3n \times 3n$ array sizes, inconsistent performance

© 2023 Wiley-VCH GmbH

21944296, 2023, 9, Downloaded from https://onlinelibrary.wiley.com/doi/10.1002/ente.202300380 by National Institute Of, Wiley Online Library on [27/11/2025]. See the Terms and Conditions (https://onlinelibrary.wiley.com/terms-and-conditions) on Wiley Online Library for rules of use; OA articles are governed by the applicable Creative Commons License

Table 1. Continued.

Ref	Approach	Category	Array	Description	Drawbacks/limitations
[24]	Optimal sudoku (OSU)	Puzzle-based, static	9 × 9	Employs the rules of optimal sudoku for the TCT-configured PV array	Incompatible for asymmetric arrays, exists several solution sets & finding optimal pattern is non-viable
[25]	Odd even (OEA)	Number-based, static	6 × 4	Follows analytical arrangement of odd and even numbers to determine reconfigured matrix	Half of the panels still remain in the same row leading to poor shade dispersion, exhibits numerous power peaks, inconsistent performance, increased mismatch losses, underperforms under many cases
[26]	Odd even prime (OEP)	Number-based, static	9 × 9	Updated version of OEA using prime numbers to determine reconfigured matrix	
[27]	New array (NA)	Logic-based, static	9 × 9	Arrange all the panels in diagonal fashion to disperse row shading	Yields highly unsatisfactory performance due to high correlation between diagonal panels
[28]	Diagonal TCT (DT)	Shift-based, static	4 × 4	Reconfigures the conventional TCT PV array based on shifting operations	Exhibits very poor performance under diagonal shading, low power enhancement
[29]	Multi-diagonal sudoku (MS)	Puzzle-based, static	9 × 9	Performs physical relocation based on multidiagonal sudoku pattern	Exhibits poor shade dispersion under certain shadings, not compatible for asymmetric arrays
[29]	Canonical sudoku (CS)	Puzzle-based, static	9 × 9	Performs physical relocation based on canonical sudoku pattern	Increased row current mismatch, inconsistent performance, not scalable
[30]	Complementary sudoku	Puzzle-based, static	6 × 6	Physical relocation based on complementary sudoku puzzle pattern	Quite low power enhancement wrt others, not compatible for asymmetric arrays
[31]	Advanced sudoku (AS)	Puzzle-based, static	9 × 9	Performs physical relocation based on advanced Sudoku pattern	Not scalable for asymmetric arrays, exists several solution sets and finding optimal pattern is non-viable
[32]	Chaos map (CM)	Mapping, static	6 × 6, 7 × 7	Sensorless and switchless reconfiguration strategy inspired by Image processing	Incompatible for asymmetric arrays, poor shade dispersion, exhibit many MPPs
[33]	Spiral pattern array (SPA)	Pattern-based, static	9 × 9	Reconfigured the array based on spiral step pattern for mismatch alleviation	Inconsistent performance, Ineffective under diagonal shading, not verified for asymmetric arrays
[34]	Non-symmetrical Pattern (NP)	Analytical, static	9 × 9	Reconfiguration is based on interchanging the rows while maintaining the columns constant	Limited analysis, efficiency compared only with TCT, algorithm is not tested for asymmetric arrays
[35]	Henon map (HM)	Mapping, static	9 × 9, 3 × 5	Employs Hénon chaotic map for restructuring to minimize row current difference	Not efficient under column shade, low power enhancement
[36]	Twisted two-step	Repositioning, static	9 × 9	Performs panel swapping in z sequence to reconfigure the array	Poor shade dispersion during column shading, underperforms under many shading conditions

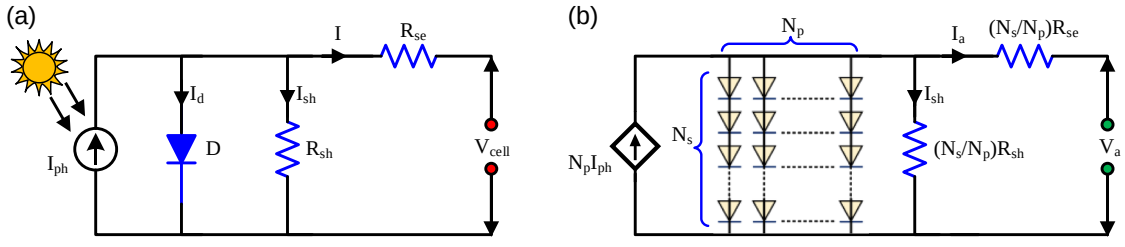

Figure 1. Equivalent-circuit model of a) PV cell and b) PV array.

where E_{go} represents the bandgap energy of the semiconductor material, and I_{rs} represent the reverse saturation cell current under normal conditions. Replacing I_{sh} and I_d in Equation (1), then

© 2023 Wiley-VCH GmbH

21944296, 2023, 9, Downloaded from https://onlinelibrary.wiley.com/doi/10.1002/ente.202300380 by National Institute Of, Wiley Online Library on [27/11/2025]. See the Terms and Conditions (https://onlinelibrary.wiley.com/terms-and-conditions) on Wiley Online Library for rules of use; OA articles are governed by the applicable Creative Commons License

$$I_{pv} = I_{ph} - I_0\left[\exp\left(q\frac{V_{pv} + I_{pv}R_{se}}{AKT} - 1\right)\right] - \frac{V_{pv} + I_{pv}R_{se}}{R_{sh}} \quad (5)$$

where I_o represents saturation current, q represents the charge of electron, V_{cell} represents cell output voltage, R_{se}, R_{sh} represent series and shunt resistance, K represents Boltzmann's constant, T represents operating temperature, and A represents ideality factor.

Since the average PV cell only produces about 3.5 W at 0.6 V, substantial power can be obtained by connecting numerous solar cells in a series and parallel configuration. The PV arrays are made up of many PV modules that have been installed and can be configured by connecting them in series and parallel. PV array configuration is determined by the power plant's desired rated voltage and current. If N_s cells in series and N_p cells in parallel are connected, the equation for I_{pv} can be stated as follows

$$I_{pv} = N_p I_{ph} - N_p I_0\left[\exp\left(q\frac{V_{pv} + I_{pv}R_{se}}{N_s AKT} - 1\right)\right] - \frac{N_p V_{pv} + N_s I_{pv} R_{se}}{N_s R_{sh}} \quad (6)$$

The efficiency of the PV module is minimally sensitive to variations in parallel resistance (R_{sh}) and extremely sensitive to small variations in series resistance (R_{se}). As a result, shunt resistance is considered to be open, and by assigning shunt resistance to infinity ($R_{sh} = \infty$), the new equation for I_{pv_cell} is obtained as follows

$$I_{pv} = N_p\left[I_{ph} - I_0\left[\exp\left(q\frac{V_{pv} + I_{pv}R_{se}}{N_s AKT} - 1\right)\right]\right] \quad (7)$$

As the series resistance is indeed very low (between 0.005 and 0.01), the values of R_{se} and R_{sh} are disregarded by setting R_{se} to 0 and R_{sh} to ∞. In an ideal solar cell, there would be no series resistance, no series losses, and no leaking to the ground. The expression for the ideal PV cell I–V characteristics is simplified and is given as follows for a single ideal cell

$$I_{pv} = I_{ph} - I_0\left[\exp\left(q\frac{V_{pv}}{AKT} - 1\right)\right] \quad (8)$$

3. Proposed Methodology

In mathematics, an integer number sequence is an ordered series of integers. It can be defined explicitly by assigning a formula for its mth term or indirectly by providing a correlation between its terms. There are many such integer sequences available, among which the Fibonacci sequence[40] is well-regarded. Further, the Fibonacci sequence has the unique property that a 2×2 matrix formed by any four consecutive terms is a unimodular matrix and is periodic and hence can be considered as an image scrambler that can be employed in image encryption to encrypt the image by decorrelating its adjacent pixels.[41] The sequence is described as follows.

3.1. Fibonacci Sequence and Its Transform

Consider (n) and (n) to be the respective numbers of adults and juveniles of a hypothetical population with the dynamics presented by the recursive equations as follows

$$\left.\begin{aligned} X(n+1) &= X(n) + Y(n) \\ Y(n+1) &= X(n) \end{aligned}\right\} \quad (9)$$

with $X(0) = 1$ and $Y(0) = 0$. The system of equations in Equation (9) can be written in the form $X(n+1) = X(n) + X(n-1)$, which is evidently the Fibonacci recursive equation for the Fibonacci series. Equation (9) can be written in the matrix form as follows

$$\begin{bmatrix} X(n+1) \\ Y(n+1) \end{bmatrix} = \begin{bmatrix} 1 & 1 \\ 1 & 0 \end{bmatrix}\begin{bmatrix} X(n) \\ Y(n) \end{bmatrix} \quad (10)$$

Equation (10) generates the Fibonacci sequence regardless of the initial values of the vector $\begin{bmatrix} X(0) \\ Y(0) \end{bmatrix}$. As the examples are the following. If the initial values are (0) = 1 and (0) = 0, then by Equation (10), the following sequence is obtained

$$\begin{aligned} \begin{bmatrix} 1 \\ 0 \end{bmatrix} \to \begin{bmatrix} 1 & 1 \\ 1 & 0 \end{bmatrix}\begin{bmatrix} 1 \\ 0 \end{bmatrix} = \begin{bmatrix} 1 \\ 1 \end{bmatrix} \to \begin{bmatrix} 1 & 1 \\ 1 & 0 \end{bmatrix}\begin{bmatrix} 1 \\ 1 \end{bmatrix} = \begin{bmatrix} 2 \\ 1 \end{bmatrix} \\ \to \begin{bmatrix} 1 & 1 \\ 1 & 0 \end{bmatrix}\begin{bmatrix} 2 \\ 1 \end{bmatrix} = \begin{bmatrix} 3 \\ 2 \end{bmatrix} \to \begin{bmatrix} 1 & 1 \\ 1 & 0 \end{bmatrix}\begin{bmatrix} 3 \\ 2 \end{bmatrix} = \begin{bmatrix} 5 \\ 3 \end{bmatrix} \\ \to \begin{bmatrix} 1 & 1 \\ 1 & 0 \end{bmatrix}\begin{bmatrix} 5 \\ 3 \end{bmatrix} = \begin{bmatrix} 8 \\ 5 \end{bmatrix} \end{aligned} \quad (11)$$

or by considering $X(0) = 0$ and $Y(0) = 1$, the obtained sequence is

$$\begin{aligned} \begin{bmatrix} 0 \\ 1 \end{bmatrix} \to \begin{bmatrix} 1 & 1 \\ 1 & 0 \end{bmatrix}\begin{bmatrix} 0 \\ 1 \end{bmatrix} = \begin{bmatrix} 0 \\ 1 \end{bmatrix} \to \begin{bmatrix} 1 & 1 \\ 1 & 0 \end{bmatrix}\begin{bmatrix} 1 \\ 0 \end{bmatrix} = \begin{bmatrix} 1 \\ 1 \end{bmatrix} \\ \to \begin{bmatrix} 1 & 1 \\ 1 & 0 \end{bmatrix}\begin{bmatrix} 1 \\ 1 \end{bmatrix} = \begin{bmatrix} 2 \\ 1 \end{bmatrix} \to \begin{bmatrix} 1 & 1 \\ 1 & 0 \end{bmatrix}\begin{bmatrix} 2 \\ 1 \end{bmatrix} = \begin{bmatrix} 3 \\ 2 \end{bmatrix} \\ \to \begin{bmatrix} 1 & 1 \\ 1 & 0 \end{bmatrix}\begin{bmatrix} 3 \\ 2 \end{bmatrix} = \begin{bmatrix} 5 \\ 3 \end{bmatrix} \to \begin{bmatrix} 1 & 1 \\ 1 & 0 \end{bmatrix}\begin{bmatrix} 5 \\ 3 \end{bmatrix} = \begin{bmatrix} 8 \\ 5 \end{bmatrix} \end{aligned} \quad (12)$$

The Fibonacci sequence $\{F_n\}$ or Fibonacci numbers, F_n are described by the recurrence relation[40] as follows

$$F_n = \begin{cases} 0 & \text{if } n = 0 \\ 1 & \text{if } n = 1 \\ F_{n-1} + F_{n-2} & \text{if } n \geq 2 \end{cases} \quad (13)$$

The above identity in Equation (11) is well-known as the Cassini formula. Besides, the Fibonacci sequence can be extended backward as follows

© 2023 Wiley-VCH GmbH

21944296, 2023, 9, Downloaded from https://onlinelibrary.wiley.com/doi/10.1002/ente.202300380 by National Institute Of, Wiley Online Library on [27/11/2025]. See the Terms and Conditions (https://onlinelibrary.wiley.com/terms-and-conditions) on Wiley Online Library for rules of use; OA articles are governed by the applicable Creative Commons License

$$F_{-n} = F_{-n+2} - F_{-n+1} = (-1)^{n+1} F_n, \text{for } n \geq 2 \tag{14}$$

The Fibonacci series starting from zero is given by the following

n	0	1	2	3	4	5	6	7	8	9	10	11	.....
F_n	0	1	1	2	3	5	8	13	21	34	55	89	.....

$$\text{and } F^n = \begin{bmatrix} F_{n+1} & F_n \\ F_n & F_{n-1} \end{bmatrix}; F^1 = \begin{bmatrix} 1 & 1 \\ 1 & 0 \end{bmatrix}; F^2 = \begin{bmatrix} 2 & 1 \\ 1 & 1 \end{bmatrix} \tag{15}$$

Equation (11) is a linear recurrence equation $x_n = Ax_{n-1} + Bx_{n-2}$ where $n \geq 3$, thus the closed form of F_n is given by $F_n = \frac{\alpha^n - \beta^n}{\alpha - \beta}$, where α and β are the roots of $x^2 = Ax + B$. Since $A = B = 1$, the characteristic equation becomes $x^2 - x - 1 = 0$ with roots $x = \left(\frac{1 \pm \sqrt{5}}{2}\right)$. The closed form is now obtained by $F_n = \frac{(1+\sqrt{5})^n - (1-\sqrt{5})^n}{2^n \sqrt{5}}$. This is called Binet's formula,[37] named after the French mathematician Binet. Fibonacci numbers F_n can be written as $\frac{\varnothing^n - (-\varnothing)^{-n}}{\sqrt{5}}$, $n = 0, \pm 1, \pm 2, \pm 3, \pm 4 \ldots$, where $\varnothing = \left(\frac{1+\sqrt{5}}{2}\right)$, which is termed a golden ratio (golden mean/golden proportion/ golden section/ divine proportion). The golden ratio '$\varnothing$' is the ratio of the consecutive numbers $\left(\lim_{n} \frac{F_n}{F_{n-1}} = \varnothing\right)$ in the Fibonacci sequence tending towards an irrational number which is about 1.61803398874.

A formal image encryption approach employs transformation matrices to relocate the pixels of an image.[42] The transformation matrices formed by the integer sequences decorrelates the pixels effectively. The Fibonacci sequence-based transform maintains uniformity spreading all the adjacent pixels in such a way that they are all equidistant to each other, promising the most satisfactory encryption. It is noted that a 2×2 matrix constructed by any four successive numbers of the Fibonacci sequence is a unimodular matrix that effectively relocates the pixel coordinates of a matrix and, therefore, can be considered for image scrambling through encryption. The generalized form of FT is a mapping $F: T^2 \rightarrow T^2$ and can be described as follows

$$\begin{bmatrix} x(i+1) \\ y(i+1) \end{bmatrix} = \begin{bmatrix} \mathrm{F_i} & \mathrm{F_{i+1}} \\ \mathrm{F_{i+2}} & \mathrm{F_{i+3}} \end{bmatrix} \begin{bmatrix} x(i) \\ y(i) \end{bmatrix} \bmod \mathrm{N} \tag{16}$$

where x and $y \in \{0, 1, 2, 3, \ldots . N-1\}$, x(i), y(i) are the old coordinates, and $x(i+1)$, y(i + 1) are the new coordinates of the matrix, F_i is ith term in a Fibonacci sequence, "mod" is the modulo operator and N is the size of a digital image. So, by using Fibonacci transformation matrix, the old coordinates of the matrix are replaced by the new ones. By denoting $\begin{bmatrix} \mathrm{F_i} & \mathrm{F_{i+1}} \\ \mathrm{F_{i+2}} & \mathrm{F_{i+3}} \end{bmatrix}$ as $\mathrm{FT_i}$, the first and second transformation matrices of the Fibonacci sequence are given as follows

$$\mathrm{FT1} = \begin{bmatrix} \mathrm{F_1} & \mathrm{F_2} \\ \mathrm{F_3} & \mathrm{F_4} \end{bmatrix} = \begin{bmatrix} 0 & 1 \\ 1 & 2 \end{bmatrix}, \mathrm{FT2} = \begin{bmatrix} \mathrm{F_2} & \mathrm{F_3} \\ \mathrm{F_4} & \mathrm{F_5} \end{bmatrix} = \begin{bmatrix} 1 & 1 \\ 2 & 3 \end{bmatrix} \tag{17}$$

Similarly, many more forms of the transformation matrix of Fibonacci series for distinct values of 'i' can be obtained. Furthermore, by iterating Equation (12) with the following procedure, the scrambling effect is further enhanced.

$$\begin{bmatrix} x(i+1) \\ y(i+1) \end{bmatrix} = \begin{bmatrix} \mathrm{F_i} & \mathrm{F_{i+1}} \\ \mathrm{F_{i+2}} & \mathrm{F_{i+3}} \end{bmatrix}^n \begin{bmatrix} x(i) \\ y(i) \end{bmatrix} \bmod \mathrm{N},\ 0\ n \geq 2 \tag{18}$$

The pseudocode of FT scrambling is shown in **Figure 2**. **Figure 3**a depicts the squares arranged in a spiral fashion oriented anticlockwise having the edge lengths given by the Fibonacci series. The most fascinating property of Pascal's triangle is that the sequence of the sum of the numbers of its diagonals is the Fibonacci recurrence sequence which is shown in Figure 3b.

3.2. Image Quality Metrics for Performance Assessment

Since the proposed technique can be employed as an image scrambler in the image encryption process, it can be best evaluated using the image quality performance indices,[43] as shown in **Table 2**. A good encryption algorithm will manifest the lowest correlation, highest mean square error (MSE), lowest structural similarity index measure (SSIM), and peak signal-to-noise ratio (PSNR) values. The least correlation indicates the maximum extent to which the algorithm has decorrelated the adjacent pixels. The considered original image and corresponding resultant encrypted image obtained by proposed strategy are shown in **Figure 4**.

Generalized Fibonacci Transform Scrambling

```
// (X, Y) are matrix coordinates
// R and C- rows and columns
// K is Matrix size

Process of FT encryption
    1: Input: Matrix of size rows, column
    2: Output: Optimal rearranged matrix
    3: tot_moves = abs(rows - columns) + 1;
    4: K = min(rows, columns);
    5: Initialize coordinates (X , Y) =(0 , 0);
    6: while (termination criteria is not met) do
    7: for i = 1 to tot_moves do
    8:     FT(matrix, X, Y, K, i)
    9:     if rows < columns then
   10:         do increment the X-coordinate number
   11:     else
   12:         do increment the Y-coordinate number
   13: end for
   14: FT (matrix, X, Y, K)
   14: for x = X to X + (K-1) do
   15:     for y = Y to Y + (K-1) do
   16:         updation of new X-coordinate acc to Eq.(13)
   17:         updation of new Y-coordinate acc to Eq.(18)
   18:         Swap old coordinates of the matrix with the new ones
   19:     end for
   20: end for
   21: end while
end procedure
```

Figure 2. Pseudocode of generalized FT scrambling.

© 2023 Wiley-VCH GmbH

21944296, 2023, 9, Downloaded from https://onlinelibrary.wiley.com/doi/10.1002/ente.202300380 by National Institute Of, Wiley Online Library on [27/11/2025]. See the Terms and Conditions (https://onlinelibrary.wiley.com/terms-and-conditions) on Wiley Online Library for rules of use; OA articles are governed by the applicable Creative Commons License

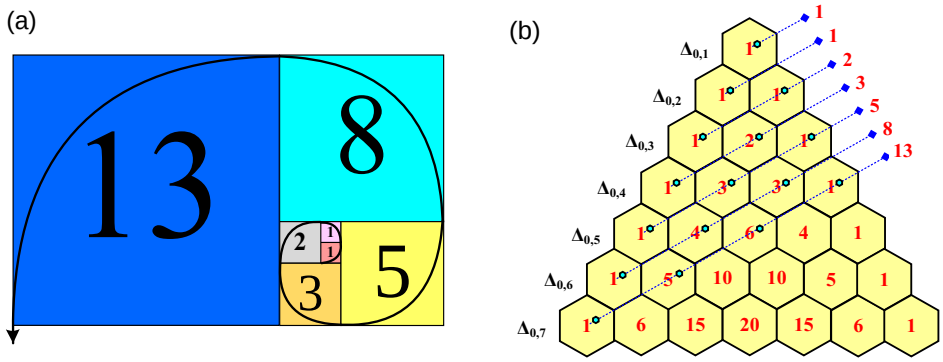

Figure 3. a) Golden spiral formed by Fibonacci series, b) Pascal's triangle Fibonacci series mapping.

Table 2. Image quality metrics[43] for evaluation.

Array	Correlation	MSE	PSNR	SSIM
9×9	+0.0396	1293.3	−31.1171	−0.0112
4×4	−0.0396	262.50	−24.1913	−0.1143
4×8	+0.0038	259.50	−24.1414	−0.0614

The higher values of MSE and the lower values of PSNR indicate the maximum error between the original and encrypted images. Besides, the lower the SSIM, the lower the structural similarity between the images. The proposed FT technique achieves the optimal values of all these indices.

3.2.1. Histogram Analysis

A graphic representation of the number of image pixels that have the same gray level is called an image histogram.[43] Thus, each vertical bar shows the number of instances of a certain color level in an image, and the *x*-axis indicates the color level, which ranges from 0 to 255. This color dispersion of an encrypted image is crucial from a cryptographic perspective since it can provide information regarding the original image. More specifically, if the original image's histogram is flat and uniform, the encrypted image neither provides characteristics of the original image nor the relationship between it and the latter. The considered original image and the corresponding resultant encrypted image are displayed in Figure 4. Further, the corresponding histogram analysis of the red, green, and blue channels of the original and encrypted images is shown in **Figure 5**. It is clearly evident from Figure 5 that the histogram of the encrypted image is flat and uniform and considerably distinguishable from the histogram of the original image. This is due to the uniform and effective dispersion of pixels in the encrypted image by the proposed scheme.

3.2.2. Correlation Analysis

Each pixel in the original image has a strong correlation with either its horizontal, vertical, or diagonal neighbor. To ensure that there is no correlation between the neighboring pixels and for its value which is popularly termed as correlation coefficient (r_{xy}) has to be almost zero, a robust cryptographic encryption algorithm must minimize this correlation.[43] The following are the mathematical formulas of the correlation coefficients

$$r_{xy} = \frac{E((x - E(x))(y - E(y)))}{\sqrt{D(x)D(y)}} \tag{19}$$

$$E(x) = \frac{1}{N}\sum_{i=1}^{N} x_i \tag{20}$$

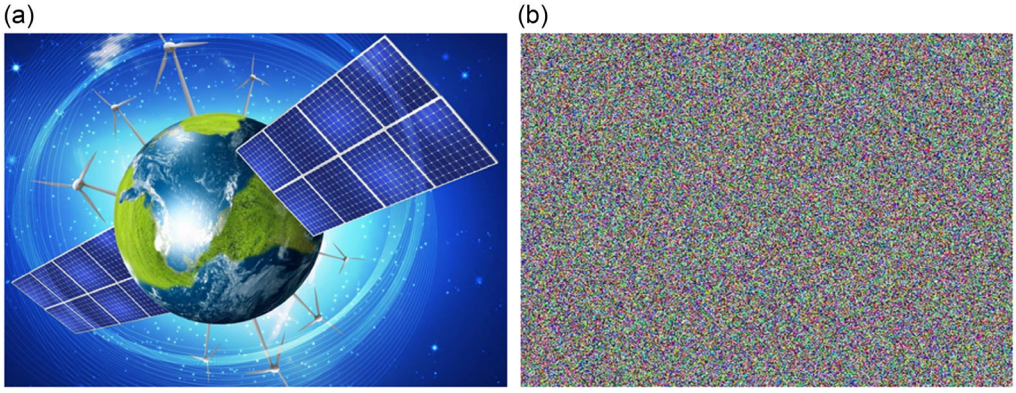

Figure 4. a) Original image and b) its respective encrypted image.

© 2023 Wiley-VCH GmbH

21944296, 2023, 9, Downloaded from https://onlinelibrary.wiley.com/doi/10.1002/ente.202300380 by National Institute Of, Wiley Online Library on [27/11/2025]. See the Terms and Conditions (https://onlinelibrary.wiley.com/terms-and-conditions) on Wiley Online Library for rules of use; OA articles are governed by the applicable Creative Commons License

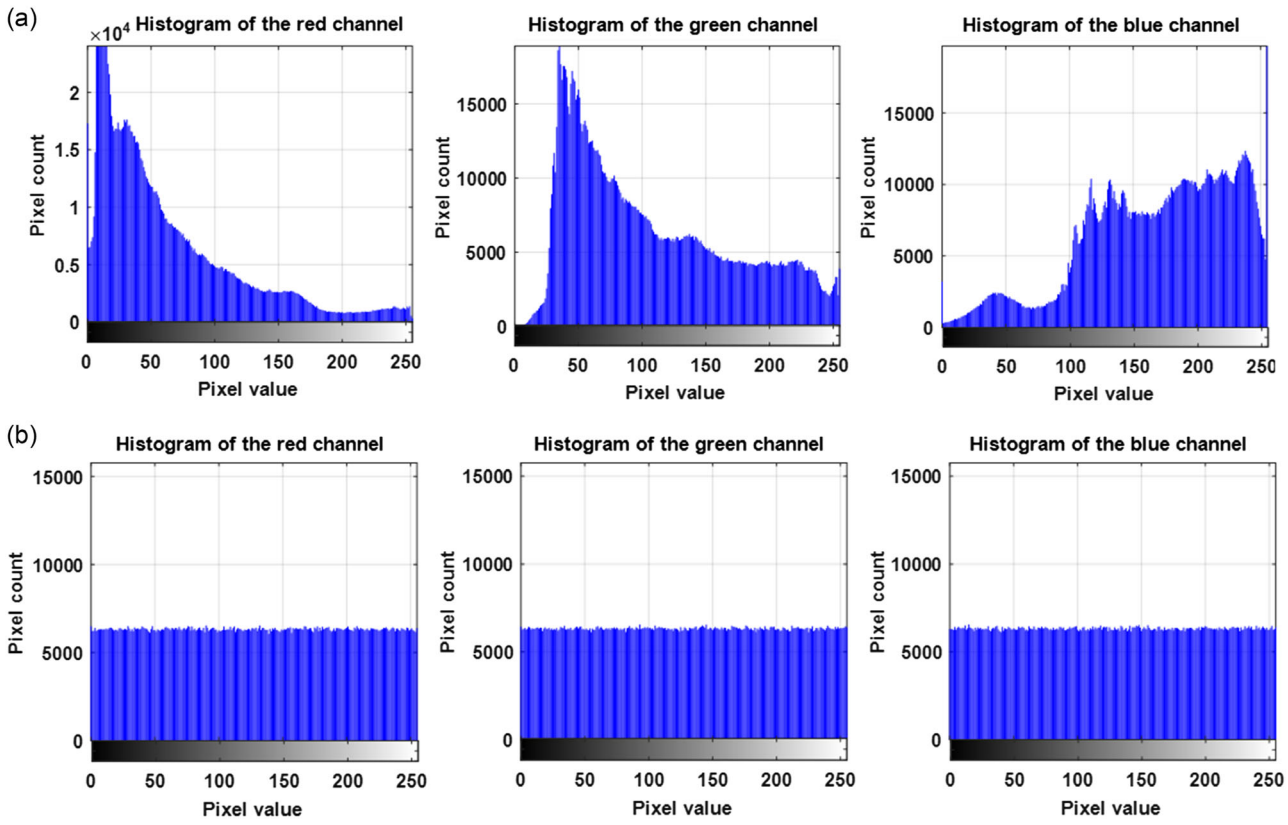

Figure 5. Histogram analysis of a) original image and b) its respective encrypted image.

$$D(x) = \frac{1}{N}\sum_{i=1}^{N}(\mathrm{x}_i - E(x))^2 \tag{21}$$

where $E(x)$ denotes the expectation and $D(x)$ denotes the variance of variable x, respectively.

The obtained results of the correlation coefficients for the original image and its corresponding encrypted image are given in Table 2. It is evident from Table 2 that the substantial correlation between the adjoining pixels in the original image is significantly lowered in the encrypted image obtained by the proposed strategy. Further, as noticed in **Figure 6** that there exists a huge correlation between the pixels in the original image, whereas there exists no observable correlation between the pixels in the encrypted image. Thus, from the flat and uniform histograms and the insignificant correlation coefficients of the adjacent pixels of the encrypted image in the diagonal, horizontal, and vertical directions, the proposed cryptographic strategy has a good capability of decorrelating the pixels facilitating the enhanced encryption process.

3.3. Application of FT Technique in Reconfiguration

The 2×2 transformation matrices formed by any four consecutive terms of Fibonacci series encrypt the image by relocating its pixels. For instance, it is observed from Figure 4a that the blue pixels and green pixels are grouped together, and when applied with FT, all the pixel coordinates are scrambled, effectively attaining the least correlation between the adjacent pixels of the encrypted image. As the image is comprised of many pixels grouped together (Figure 4a), the solar PV array is also composed of solar panels interconnected in series and parallel to acquire the rated output. The encryption process using FT is employed here by regarding a single panel as a pixel of the image and the entire PV array as the image containing pixels. The panels of the array are configured based on the reconfigured matrix patterns acquired by FT to distribute the shade uniformly over the array for mitigating the row current variation.

3.4. Development of Integer Sequence-Based Reconfiguration

The array is optimally interconnected using a predefined configuration pattern obtained by FT technique without altering the electrical circuitry. This mitigates the shading impact without inducing any disparity in its electrical properties. The panels of the TCT-configured array are physically relocated based on rearranged FT matrix, and the structural topology distinction in the arrangements of TCT and the proposed FT is shown in **Figure 7**. It is noted from Figure 7a that panel number "24" is in the 2nd row and 4th column in TCT, and based on rearranged FT matrix, this panel is physically relocated to the 1st row and 3rd column, i.e., in between Node-A and Node-B as shown in Figure 7b. Likewise, all the panels are optimally reconfigured based on the obtained FT matrix to disseminate the shade uniformly. Considering if the first row of the FT-reconfigured array with panel numbers 44, 14, 24, and 34 experiences shading. The row-shading is now distributed to all rows as these panels are physically placed

© 2023 Wiley-VCH GmbH

21944296, 2023, 9, Downloaded from https://onlinelibrary.wiley.com/doi/10.1002/ente.202300380 by National Institute Of, Wiley Online Library on [27/11/2025]. See the Terms and Conditions (https://onlinelibrary.wiley.com/terms-and-conditions) on Wiley Online Library for rules of use; OA articles are governed by the applicable Creative Commons License

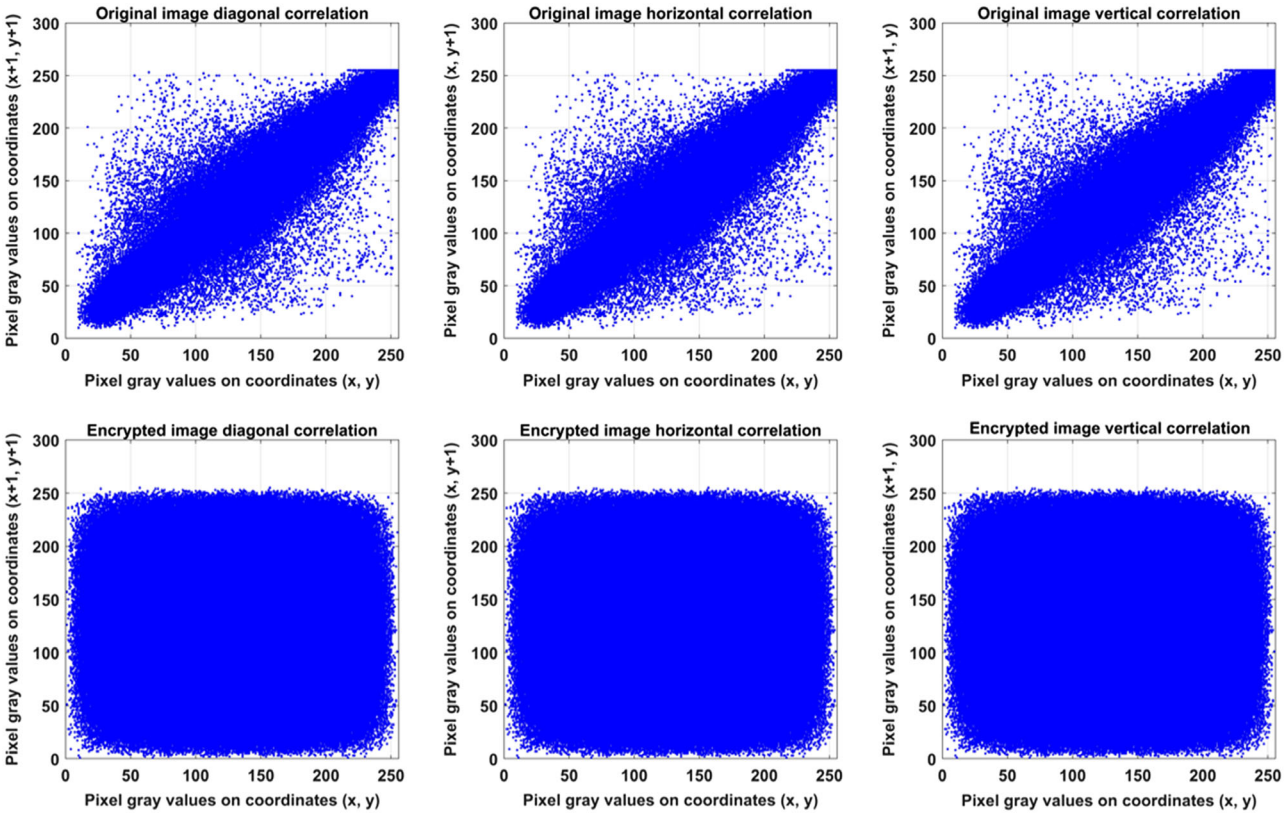

Figure 6. Correlation plots of original and encrypted images in diagonal, horizontal, and vertical directions.

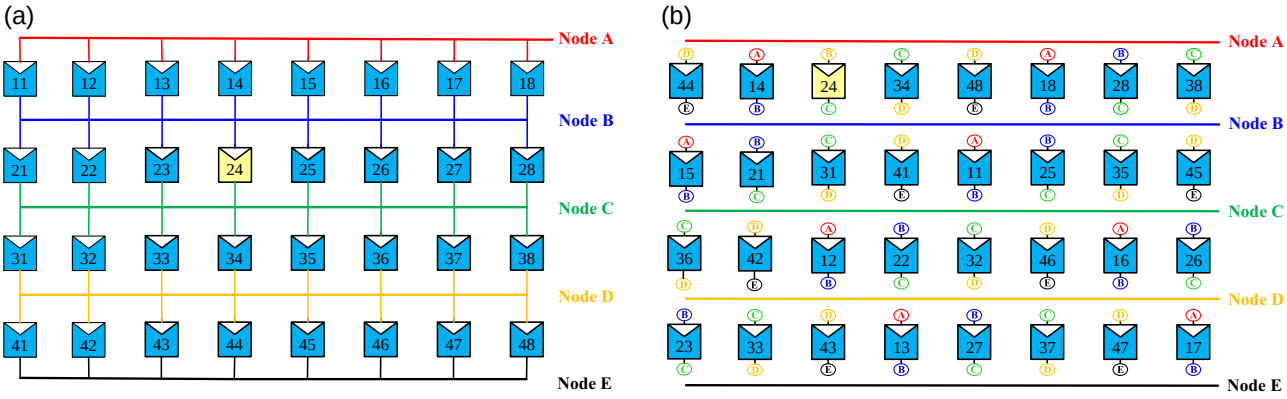

Figure 7. a) Conventional TCT and b) proposed FT-based 4 × 8 array topologies.

in the first row but are electrically connected to different rows of an array, thereby equalizing the irradiation between the rows. As a result, the proposed integer sequence-based array reconfiguration approach mitigates the row-current mismatch.

3.5. Levenberg–Marquardt Algorithm

The Levenberg–Marquardt technique, which was developed for minimizing functions that are the summation of squares of nonlinear functions, is derived from Newton's method, whereas back-propagation is the steepest descent method.[44] The LM method solves an equational system with the following form

$$F(x) = 0 \tag{22}$$

where F is a function of x with vector values, and x is an array of unknowns. Finding the x values with the lowest aggregate of the squares of $F(x)$ elements is the goal. The LM algorithm employs a combination of the steepest descent and Gauss–Newton techniques to iteratively change the values of x to minimize the

© 2023 Wiley-VCH GmbH

21944296, 2023, 9, Downloaded from https://onlinelibrary.wiley.com/doi/10.1002/ente.202300380 by National Institute Of, Wiley Online Library on [27/11/2025]. See the Terms and Conditions (https://onlinelibrary.wiley.com/terms-and-conditions) on Wiley Online Library for rules of use; OA articles are governed by the applicable Creative Commons License

objective function. By minimizing the quadratic approximation to F about the most present estimate of x, it solves a linearized form of the problem at each iteration. A damping factor is added diagonally to the Hessian matrix to make the system of linear equations that has to be solved. For a variety of nonlinear situations, the LM methodology has been found to be a dependable and effective optimization technique. It is especially beneficial for issues where the Gauss–Newton approach might not converge or behave erratically.

3.5.1. Training Process

Overall, 70% of the total data are used for training and the remaining 30% of data are used equally for testing and validation. The number of neurons in the hidden layer of the neural network is taken as 10, and the model is trained with Levenberg–Marquardt backpropagation algorithm (**Figure 8**). The parameters obtained by training with the Levenberg–Marquardt method are given in **Table 3**. The MSE versus epochs is shown in **Figure 9**. The obtained MSE of the training and testing data are 0.000184 and 0.000772, respectively. The coefficient of determination values of the training and testing data are 0.9833 and 0.9668, respectively. The regression plots for training, validation, and testing data are given in **Figure 10**a. The Gradient at 8 epochs, which is 0.00006551, Mu is 0.00001 and validation checks are 6, as shown in Figure 10b.

Table 3. Parameters obtained by training with the Levenberg–Marquardt method.[44]

Unit	Initial value	Stopped value	Target value
Epoch	0	27	1000
Elapsed time	–	00:00:00	–
Performance	0.0426	7.74e−06	0
Gradient	0.111	2.52e−05	1e−07
Mu	0.001	1e−06	1e + 10
Validation checks	0	6	6

4. Results and Discussion

A majority of the reconfiguration techniques have been tested for a 9×9 symmetric and a 4×8 asymmetric PV array under distinct shading conditions. The effectiveness of the proposed FT technique is validated in the MATLAB software environment. The performance of the proposed FT is compared with the existing 20 techniques of a 9×9 PV array under five distinct shading cases (**Figure 11**). A Kyocera KC175GT panel is considered for analysis. During normal and shading conditions, they receive 900, 400, and 200 W m^2, respectively. The power-voltage characteristics of 9×9 array under distinct shading cases are shown in **Figure 12**.

4.1. Analysis with 9×9 Symmetric PV Array

During Case-1, a triangular-patterned uniform shading case limiting the irradiation in the lower half of the PV array is considered. During this case, the OSU technique yielded superior performance among all the considered techniques. Followed by OSU, SPA exhibits 34.71% enhancement in GMP (from **Table 4**). Besides, the proposed FT technique also performs on par with SPA yielding an enhancement of 34.43%. Although OSU delivers the highest output in Case-1, its performance in Case-2 is comparatively inferior and significantly failed in Case-4 and Case-5, lowering the output respectively by 1.73% and 4.07% compared to TCT. Moreover, the major drawback of OSU is that it cannot be employable for asymmetric arrays. Further, in this case, the performance of SPA is slightly more than the proposed FT. Notwithstanding, it fails to offer consistency as its performance in Case-2 is quite poor, and in Case-4 and Case-5, SPA yields a 20.41% and 13.81% reduction in GMP due to its poor shade dispersal ability exhibiting highly unsatisfactory performance. Followed by FT, the effectiveness of the techniques such as SD, FP, OSA, SM, NOS, SC, IS, LOS, OEP, MS, CS, AS, and CM are nearly on par with each other, as shown in Figure 10. Besides, the existing CI, NAR, and HM enhance the GMP nearly by 26.8%. Due to its poor rearrangement of panels by OEA, the GMP enhancement is only limited to 17.8% (which is the lowest of all).

In Case-2, the proposed FT technique yields the highest GMP enhancing the output by 12.50% due to its effective shade dispersal ability. Followed by FT, the existing OSA, and IS exhibit better performance. The SD, FP, NOS, SC, LOS, CS, and AS enhance the GMP nearly by 10.18%, whereas the GMP enhancement with OEA, NA, and SPA techniques is only about 3.98%. The number-based OEP strategy generates 1.51% less GMP even compared to conventional TCT.

Under the Case-3 shading, the highest GMP is obtained by the proposed technique. The GMP obtained by FT is 10 570 W, which is 12.50% higher. The existing SPA, FP, and OSU

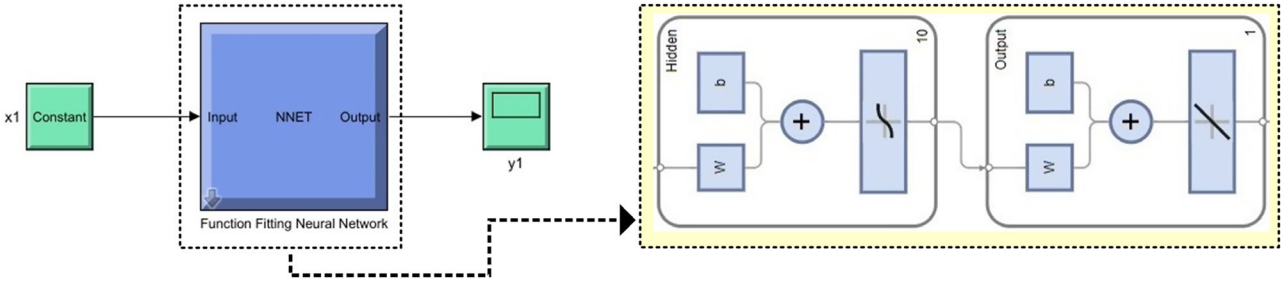

Figure 8. Levenberg–Marquardt neural network developed in MATLAB.

© 2023 Wiley-VCH GmbH

21944296, 2023, 9, Downloaded from https://onlinelibrary.wiley.com/doi/10.1002/ente.202300380 by National Institute Of, Wiley Online Library on [27/11/2025]. See the Terms and Conditions (https://onlinelibrary.wiley.com/terms-and-conditions) on Wiley Online Library for rules of use; OA articles are governed by the applicable Creative Commons License

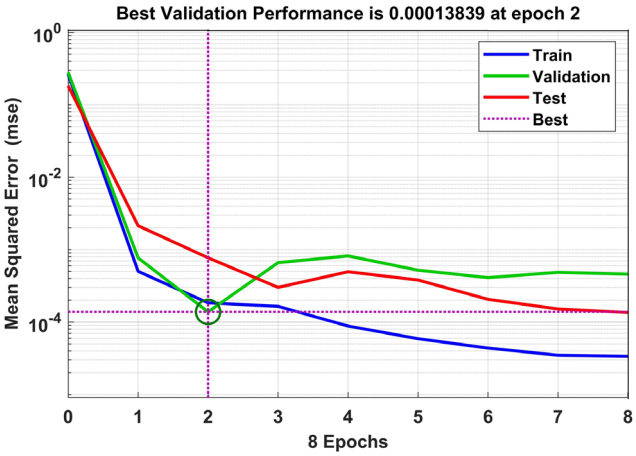

Figure 9. Mean square error versus epochs.

generate 10 555, 10 529, and 10 257 W, respectively. The other techniques, such as NAR and MS, exhibit very less improvement in GMP. Both OE and OEP yield the most unsatisfactory performance resulting in a lowered output. The shading patterns in Case-2 and Case-3 are identical except for their location in the array. It is evident from the results of these two cases shown in Table 4 that the proposed FT resulted in the same (and highest) output power enhancing the GMP by 12.50%. This is due to the fact that the FT maintains uniformity by spreading the shade of the adjacent panels ensuring that they are all equidistant to each other. Due to this intelligence in retaining uniformity while reconfiguration of panels in the array, the shade is evenly dispersed over the entire array, thereby promising consistent performance irrespective of the position of shade. On the contrary, it is clearly noted from **Figure 13** that all the existing techniques yield distinct results for the same shading pattern (when occurring at a different position), leading to inconsistent performance. For example, MS yields 10.17% gain under Case-2 and in Case-3, it yields only 3.8% gain. The SPA, which yields 12.34% gain during Case-3, exhibits only 3.9% gain during Case-2. Further, the OEA, which yields 4.2% enhancement during Case-2, now lowers the GMP by 0.65% during Case-3. This inconsistency in performance is especially due to the arbitrary reconfiguration of panels. Hence, the proposed techniques are proved to be an effective solution for intelligent array reconfiguration to uniformly disperse the shade.

During Case-4, two corners of the array are considered to be shaded with two different irradiation levels. The proposed FT technique intelligently disperses the shade minimizing the variation in the currents among the distinct rows of the PV array. The FT technique improves the GMP by 5.06%. Followed by FT, the OSA exhibit 4.99% enhancement. Further, the IS, MS, and AS offer a suboptimal performance resulting in an enhancement of only about 1.35%. Besides, due to their indiscriminate shade dispersal, all the other existing techniques, such as SD, FP, SM, CI, NOS, SC, LOS, OSU, OEA, OEP, NAR, CS, CM, and SPA, deliver quite inferior performance even compared to the conventional TCT.

The diagonal shading pattern (in Case-5) limiting the irradiation of the diagonal panels of an array is considered in Figure 11. The diagonal shading is also predominant in the practical scenario; however, it is not well considered in the previous research studies on reconfiguration. Under this case, only the proposed FT and the existing LOS, CM, and HM techniques offer optimal shade dispersion. Conversely, all the other existing techniques yield significantly reduced GMP even compared to conventional TCT, as shown in Figure 13. This reveals that the arbitrary reconfiguration leads to a significant power loss rather than gain. Indiscriminate shade dispersal triggers more additional

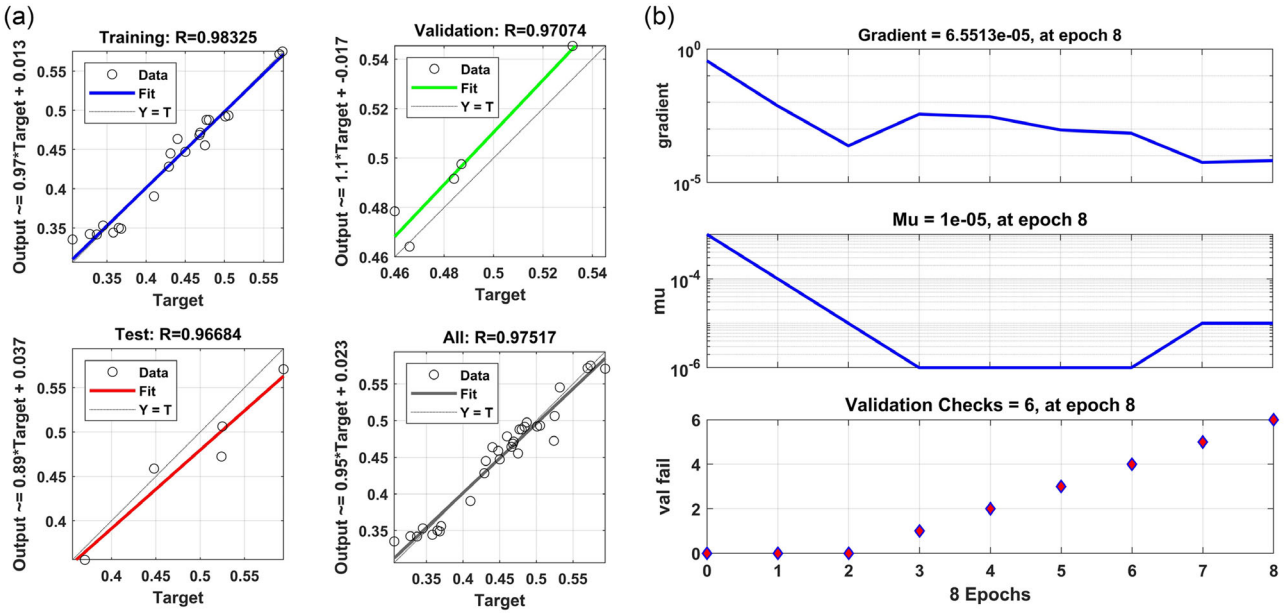

Figure 10. a) Regression plots for training, validation, and testing data b) Gradient, Mu, validation checks state.

© 2023 Wiley-VCH GmbH

21944296, 2023, 9, Downloaded from https://onlinelibrary.wiley.com/doi/10.1002/ente.202300380 by National Institute Of, Wiley Online Library on [27/11/2025]. See the Terms and Conditions (https://onlinelibrary.wiley.com/terms-and-conditions) on Wiley Online Library for rules of use; OA articles are governed by the applicable Creative Commons License

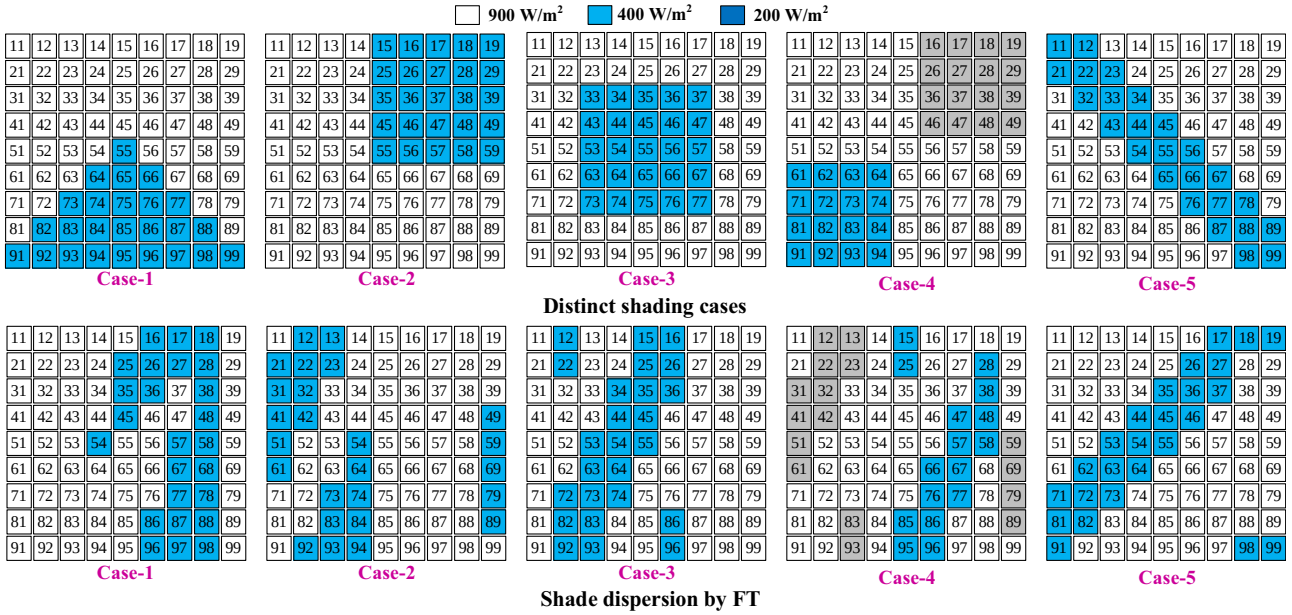

Figure 11. Distinct shading cases and respective shade dispersion by FT technique.

Table 4. GMP obtained (in watt) by various configurations for a 9×9 array.

Configuration	Case-1	Case-2	Case-3	Case-4	Case-5
TCT	7702.3	9395.7	9395.7	8825.5	10 569
SD[14]	10 260	10 352	10 273	8016.2	9783.8
FP[15]	10 257	10 354	10 552	8012.3	10 177
OSA[18]	10 352	10 552	10 260	9272.4	9679.6
NOS[18]	10 337	10 345	10 353	8578.1	10 273
SM[19]	10 337	10 170	10 145	8452.5	9691.1
CI[20]	9663.3	10 260	10 199	7727.2	9572.3
SC[21]	10 350	10 352	10 352	8673.1	9810.8
IS[22]	10 246	10 513	10 352	8943.6	9251.3
LOS[23]	10 341	10 343	10 273	8683.7	10 551
OSU[24]	10 555	10 350	10 529	8673.2	10 125
OEA[25]	9074.2	9790.7	9334.2	6424.9	9642.5
OEP[26]	10 199	9253.6	9173.9	8671.9	9775.3
NA[27]	9769.2	9769.4	9769.2	6872.8	8412.3
MS[29]	10 350	10 351	9763.0	8958.6	9810.6
CS[29]	10 296	10 351	10 269	8019.1	9712.6
AS[31]	10 212	10 347	10 260	8950.8	10 351
CM[32]	10 149	10 148	10 147	8452.6	10 569
SPA[33]	10 376	9769.2	10 555	7024.5	9097.8
HM[35]	9769.2	9395.9	9395.9	8825.5	10 569
Proposed FT	10 354	10 570	10 570	9272.4	10 569

mismatch losses compared to the existing losses. The best reconfiguration strategy is the one that should be consistent in yielding superior performance under any case of shading condition. The proposed FT technique proved its effectiveness in delivering the consistently superior performance. It is noted from Figure 12 that the PV characteristics obtained by FT are significantly enhanced, exhibiting very few MPPs. Hence, employing FT makes the task quite simple for the MPPT controllers in tracking GMP. Further, it is also evident from **Figure 14** that due to its discriminate shade dispersal, the proposed FT configuration exhibits the narrow variation in the row currents compared to the conventional TCT and hence mitigates the mismatch losses significantly.

4.2. Compatibility and Effectiveness of Proposed Technique for Asymmetric Arrays

Most of the existing static reconfiguration techniques[14–24,27–34,36] are not compatible with asymmetric arrays as they are based on puzzle-based, magic square-based, logic-based rules that are applicable only for symmetric grids. In practice, the PV arrays can be symmetrical or asymmetrical. Due to the drawbacks of these techniques, the number-based OEA[25] and OEP[26] and the chaotic-based HM[35] techniques are proposed very recently. Nevertheless, despite being compatible with asymmetric arrays, the OE, OEP, and HM techniques exhibit poor shade dispersal. To validate the effectiveness of the proposed FT technique for asymmetric arrays, a 4×8 array is considered and tested under six distinct cases, as shown in **Figure 15**.

Further, their performance has been compared with the recent OE and OEP techniques. The proposed FT technique exhibits even shade dispersion resulting in the reduced MPPs, thereby improving the PV characteristics significantly for the asymmetric arrays, as shown in **Figure 16**. Besides, due to its effective shade dispersal, FT delivers the highest GMP under all shading cases. Hence, it is noteworthy to mention that the proposed FT technique is universally compatible as well as effective under PS conditions.

© 2023 Wiley-VCH GmbH

21944296, 2023, 9, Downloaded from https://onlinelibrary.wiley.com/doi/10.1002/ente.202300380 by National Institute Of, Wiley Online Library on [27/11/2025]. See the Terms and Conditions (https://onlinelibrary.wiley.com/terms-and-conditions) on Wiley Online Library for rules of use; OA articles are governed by the applicable Creative Commons License

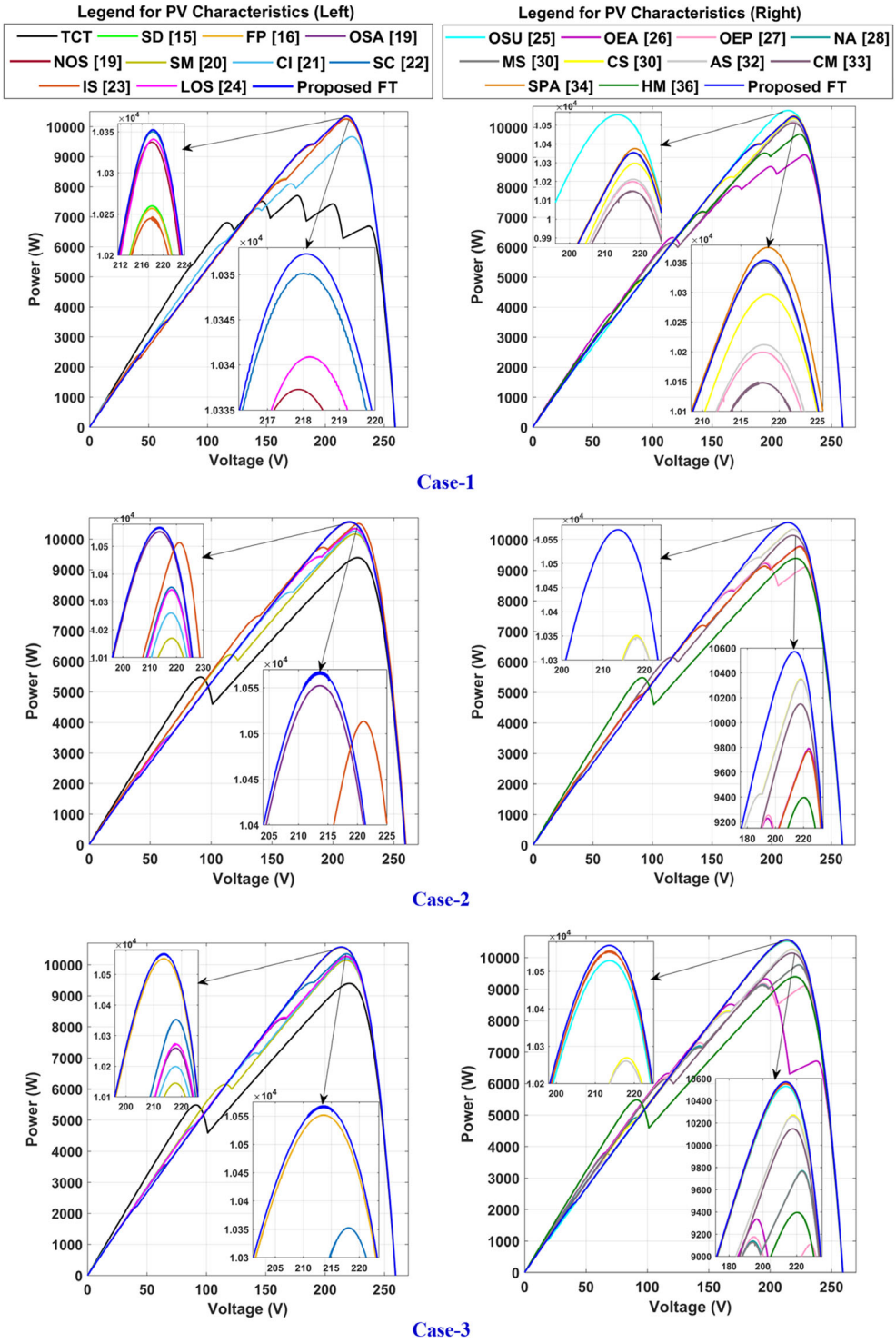

Figure 12. Power–voltage characteristics of 9 × 9 array under distinct shading cases.

4.3. Experimental Validation of Laboratory Prototype

A laboratory experimental prototype model of the proposed reconfiguration strategies is developed, as shown in **Figure 17**. The experimental test bench comprises sixteen 3 W solar panels, an artificial lighting source consisting of double-ended halogen light bulbs and a knob to vary intensity, a (300 Ω, 1.5 A) variable sliding rheostat that acts as load, banana connectors to reconfigure the array in various configurations, wires for interconnecting the panels, thick transparent sheets limiting the incident

© 2023 Wiley-VCH GmbH

21944296, 2023, 9, Downloaded from https://onlinelibrary.wiley.com/doi/10.1002/ente.202300380 by National Institute Of, Wiley Online Library on [27/11/2025]. See the Terms and Conditions (https://onlinelibrary.wiley.com/terms-and-conditions) on Wiley Online Library for rules of use; OA articles are governed by the applicable Creative Commons License

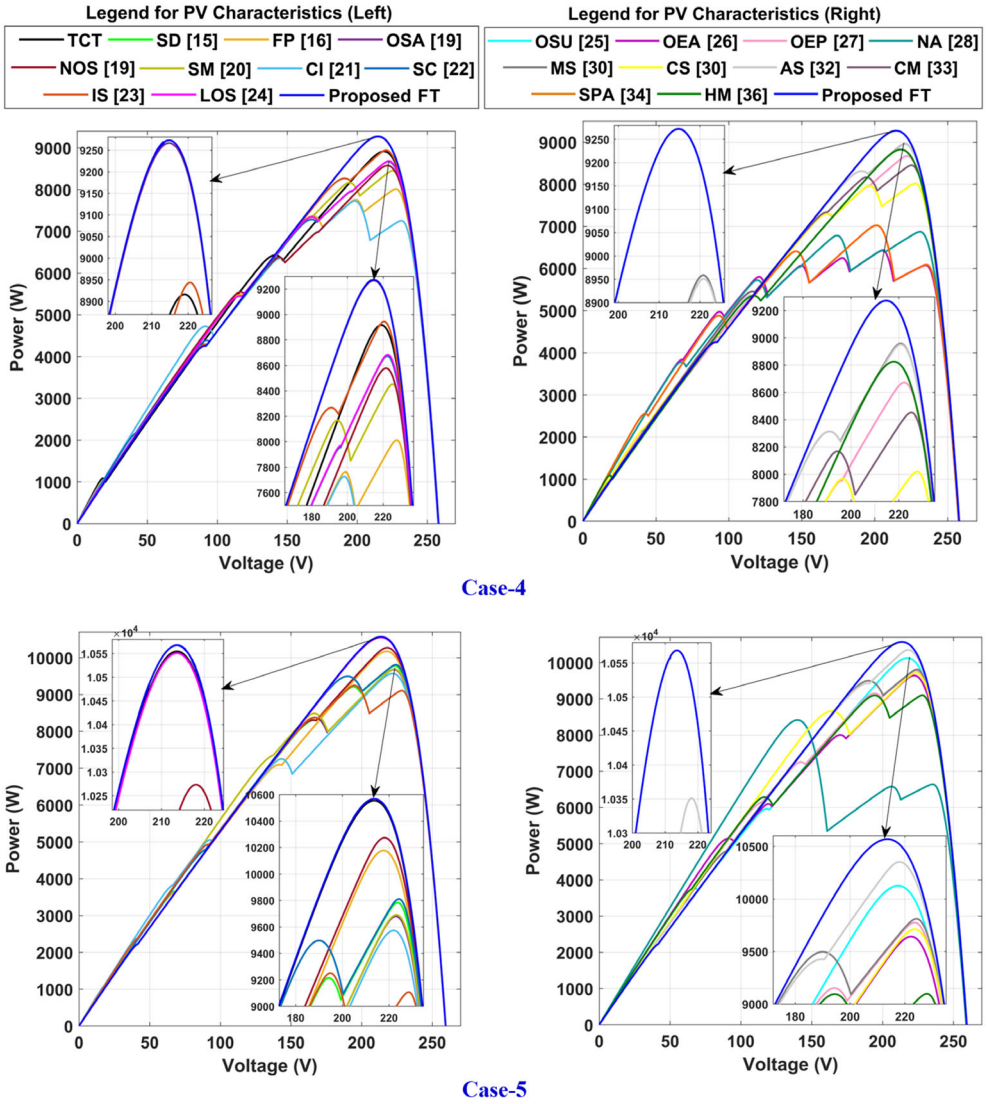

Figure 12. Continued.

irradiation to create artificial shading conditions, two SM7023A multimeters connected in series and parallel to the array to measure the array output current and voltage respectively. The uniform irradiation levels are maintained on all the panels with the proper placement of halogen bulbs over the panels. Each halogen lamp can deliver irradiation up to 400 W m^2.

The respective incident irradiation and operating temperature of the panels are measured by a portable TM-206 solar power meter and an HTD8813C infrared temperature gun. The prototype model is designed with positive and negative tappings on each module, allowing it to be reconfigured in various configurations using banana connectors. The variable rheostat connected to the array output terminals is adjusted to extract maximum power from distinct configurations of the array. There is no necessity for any additional electrical and electronic equipment/devices for hardware execution as the proposed configuration is static hence eliminating the need for sensors, switches, and other costly equipment. During normal (unshaded) operating conditions, the developed 4×4 array generates an output of 17.2 W, and the incident irradiation from the artificial lighting source is estimated to be around 330 W m^{-2}, whereas the operating temperature is found to be around 29 °C. The 4×4 PV array is connected in conventional TCT, SP[16], LS[17], DT[28], FT configurations and are tested under six shading conditions, as shown in **Figure 18**.

The unshaded and shaded panels receive the irradiations of about 300 and 150 W $m^{-2,}$ respectively. The proposed FT technique yields the highest output power during all shading cases due to its uniform dispersion of shade over the entire array resulting in minimized row current mismatch. On the contrary, the existing techniques exhibit highly inconsistent performance, as shown in **Figure 19** and **20**.

The existing DT enhances the output only in two cases (12, 14), whereas the SP and LS enhance the output in three out of six cases. This is mainly due to their arbitrary reconfiguration approach leading to indiscriminate shade dispersion. Due to this,

© 2023 Wiley-VCH GmbH

21944296, 2023, 9, Downloaded from https://onlinelibrary.wiley.com/doi/10.1002/ente.202300380 by National Institute Of, Wiley Online Library on [27/11/2025]. See the Terms and Conditions (https://onlinelibrary.wiley.com/terms-and-conditions) on Wiley Online Library for rules of use; OA articles are governed by the applicable Creative Commons License

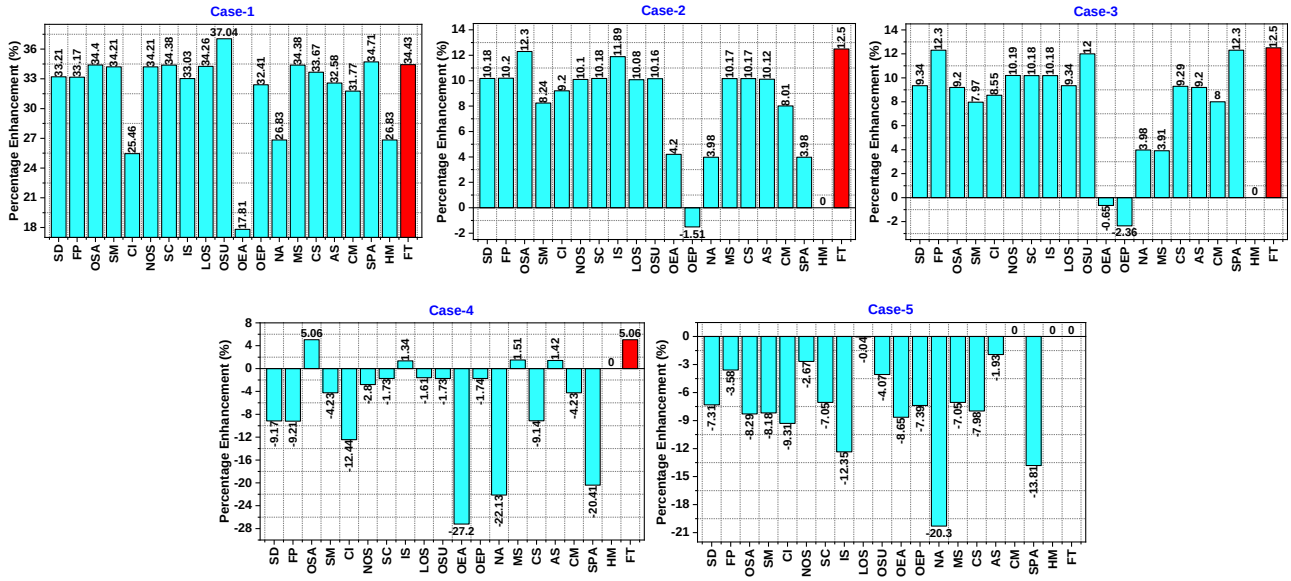

Figure 13. Percentage GMP enhancement of 9 × 9 array under Case-1 to Case-5.

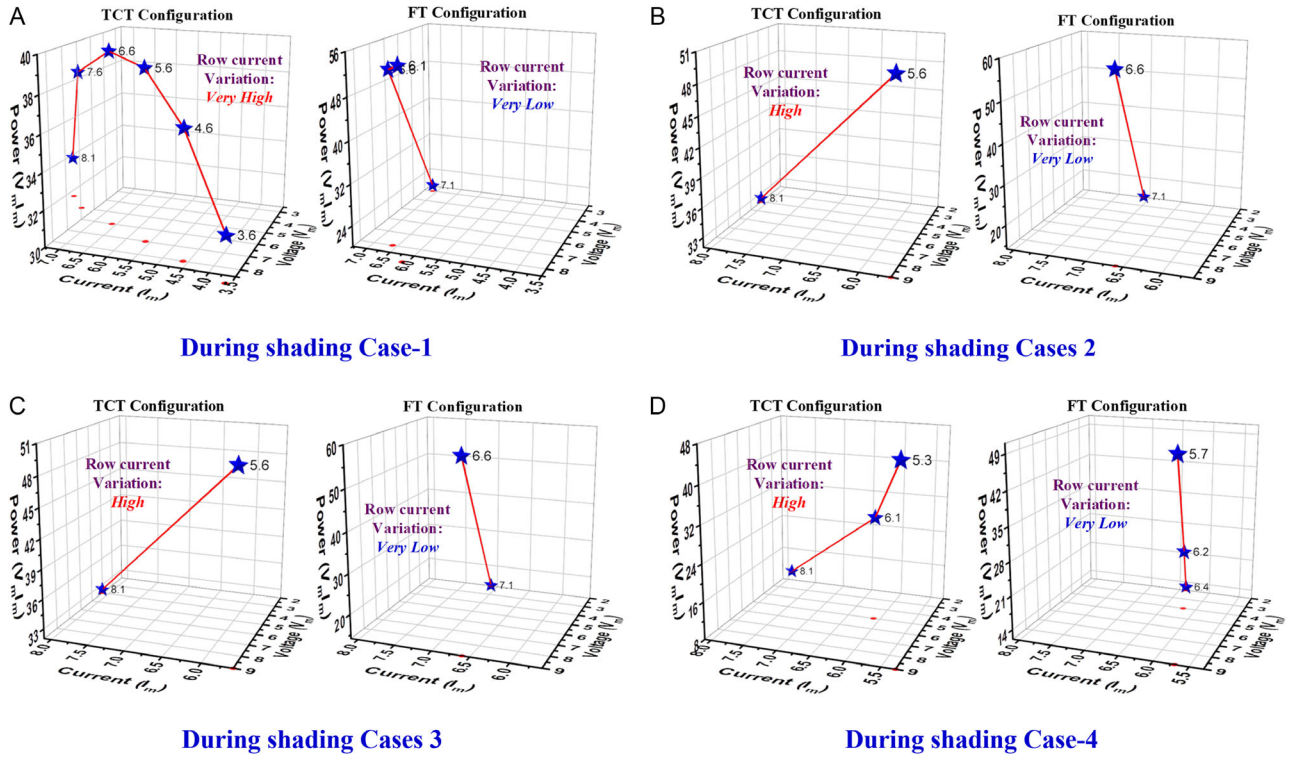

Figure 14. Row current variation under distinct shading cases of 9 × 9 array. A) during shading Case-1, B) during shading Case-2, C) during shading Case-3 and D) during shading Case-4.

the SP, LS, and DT configurations fail under diagonal shading cases-16, 17 resulting in the lowest power even compared to conventional TCT. However, the proposed FT maintains its consistency (due to its discriminate shade dispersion) in yielding superior performance in all cases, as shown in Figure 19 and 20.

4.4. Validation with Levenberg–Marquardt Neural Network MPPT

The standalone solar PV system[45] shown in **Figure 21** is simulated using the KC200GT PV module model in MATLAB

© 2023 Wiley-VCH GmbH

21944296, 2023, 9, Downloaded from https://onlinelibrary.wiley.com/doi/10.1002/ente.202300380 by National Institute Of, Wiley Online Library on [27/11/2025]. See the Terms and Conditions (https://onlinelibrary.wiley.com/terms-and-conditions) on Wiley Online Library for rules of use; OA articles are governed by the applicable Creative Commons License

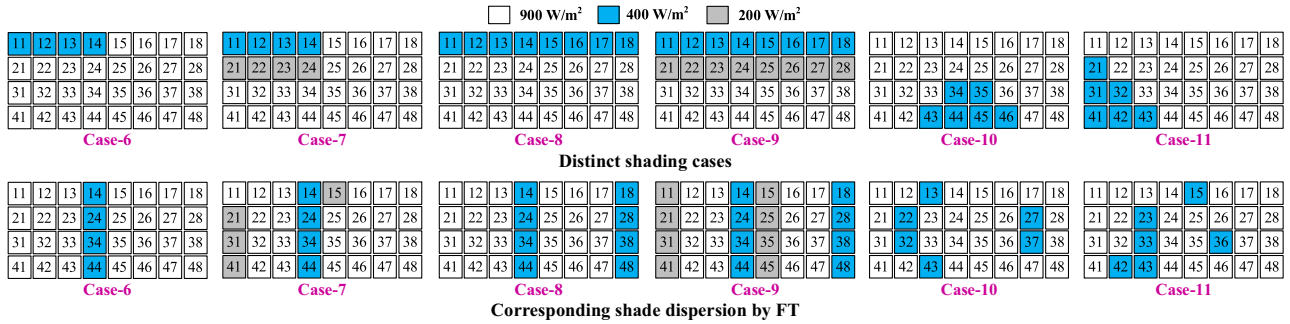

Figure 15. Distinct shading cases of 4 × 8 asymmetric array.

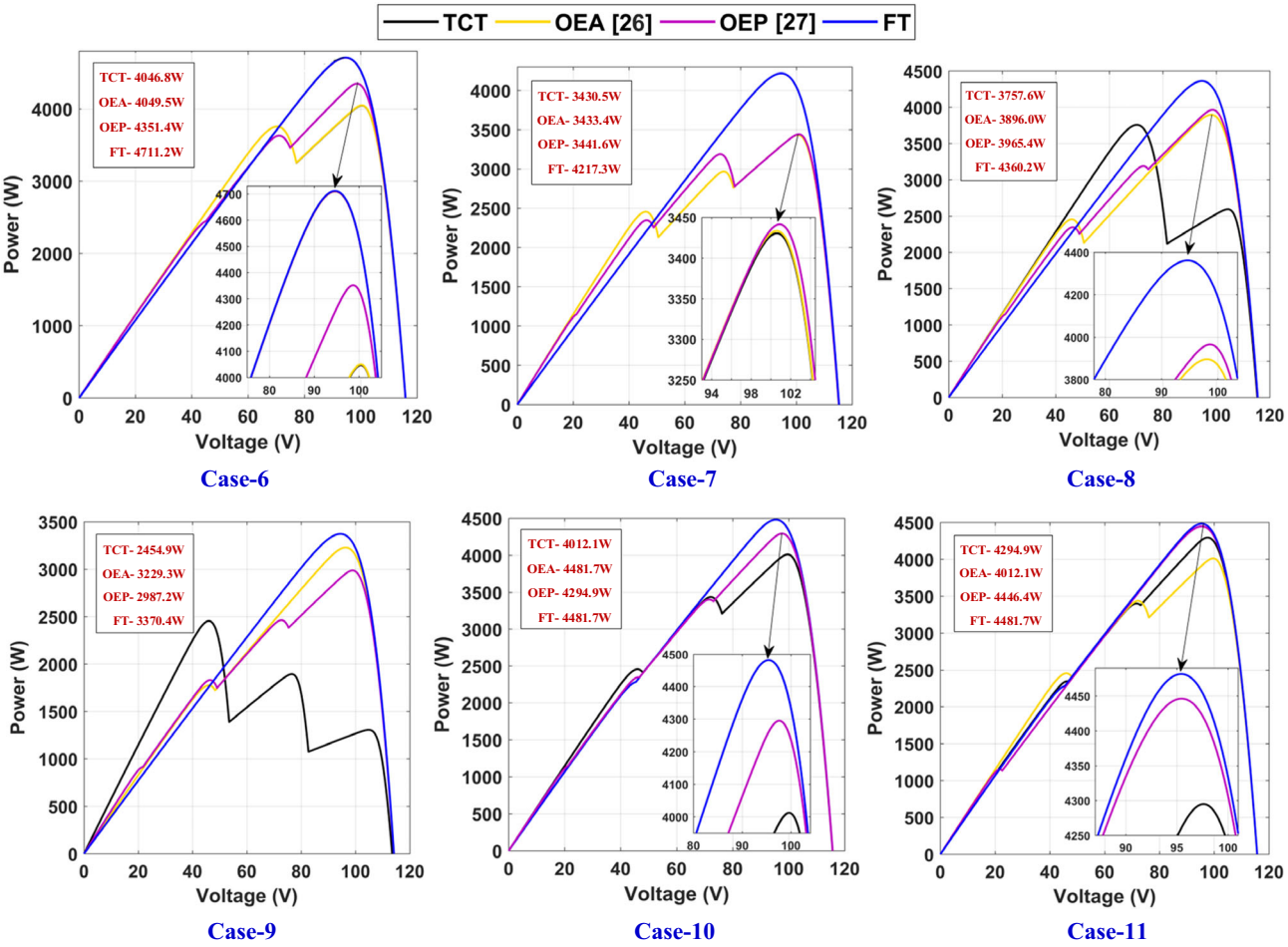

Figure 16. PV characteristics of 4 × 8 array under Case-6 to Case-11.

Simulink, and the suggested approach is programmed using MATLAB function block. This PV panel has the following electrical specifications: $V_{oc} = 32.9$ V, $I_{sc} = 8.21$ A, $V_{mpp} = 26.3$ V, and $I_{mpp} = 7.61$ A. The components of the dc-dc boost converter employed in the simulation are as follows: $L = 5.6$ mH, $C_{in} = 50$ μF, $C_o = 875$ μF, load $R_L = 12.849\ \Omega$, and the frequency of switching $f_s = 5{,}000$ Hz. To verify the effectiveness of the proposed reconfiguration algorithm, the PV system is tested for two distinct shading cases (**Figure 22**), and the obtained GMP is tracked by the Levenberg–Marquardt neural network-based MPPT controller. The advantages of integrating both the proposed reconfiguration algorithm and the neural network-MPPT controller have been detailed as follows:

During Case-18, two rows of the PV array experience shading, thereby receiving only 466 W m^2. In this case, there exists a significant mismatch of irradiations between the rows leading to MPPs in the power-voltage curves of the array. Before the

© 2023 Wiley-VCH GmbH

21944296, 2023, 9, Downloaded from https://onlinelibrary.wiley.com/doi/10.1002/ente.202300380 by National Institute Of, Wiley Online Library on [27/11/2025]. See the Terms and Conditions (https://onlinelibrary.wiley.com/terms-and-conditions) on Wiley Online Library for rules of use; OA articles are governed by the applicable Creative Commons License

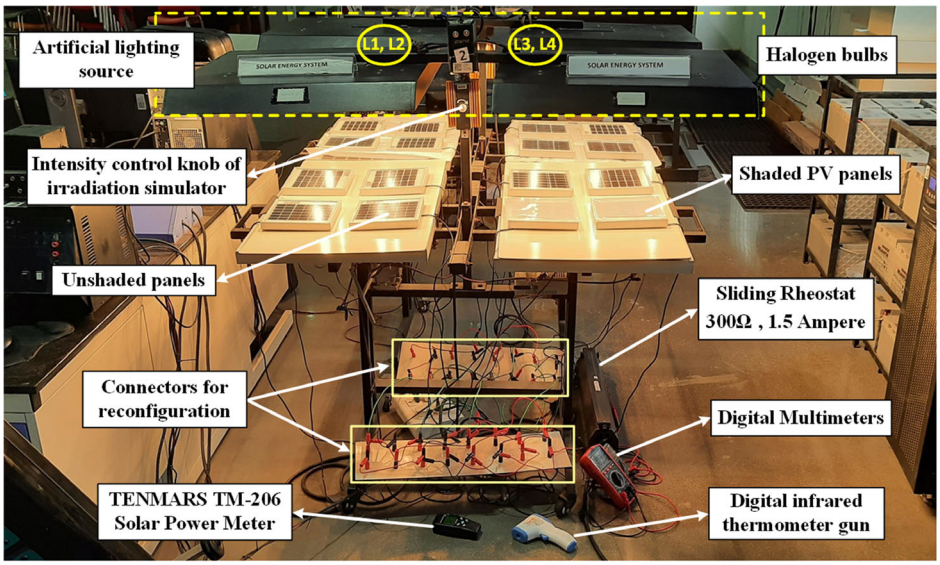

Figure 17. Laboratory prototype model of a reconfiguration system.

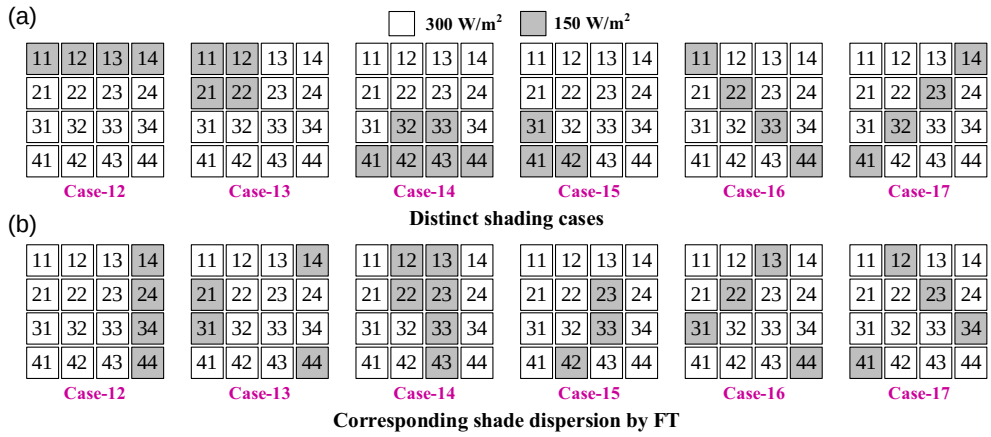

Figure 18. Distinct shading cases of 4 × 4 symmetric array. a) Distinct shading cases. b) Corresponding shade dispersion by FT.

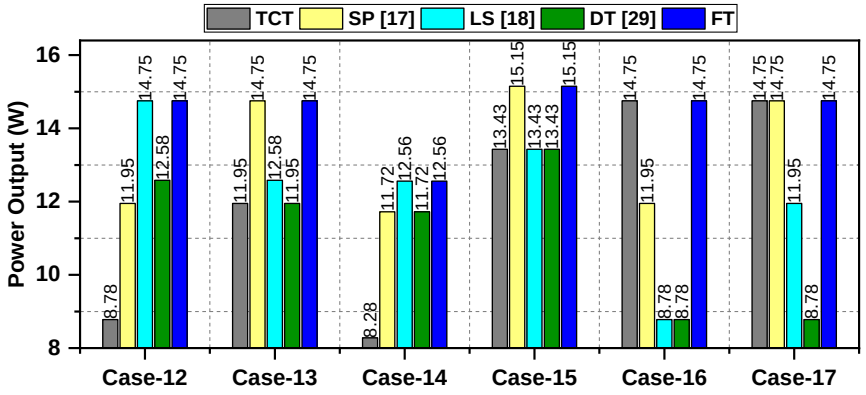

Figure 19. Power output of various configurations under shading Case-12 to Case-17.

© 2023 Wiley-VCH GmbH

21944296, 2023, 9, Downloaded from https://onlinelibrary.wiley.com/doi/10.1002/ente.202300380 by National Institute Of, Wiley Online Library on [27/11/2025]. See the Terms and Conditions (https://onlinelibrary.wiley.com/terms-and-conditions) on Wiley Online Library for rules of use; OA articles are governed by the applicable Creative Commons License

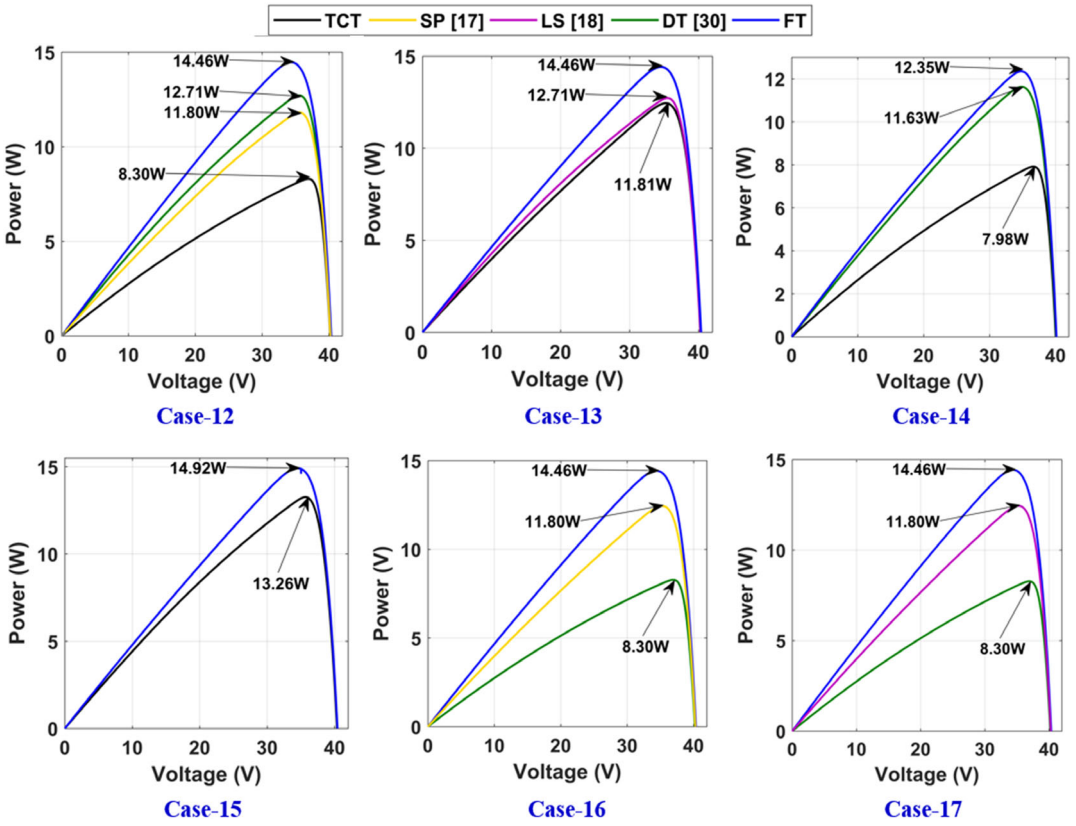

Figure 20. PV characteristics of 4 × 4 array under Case-12 to Case-17.

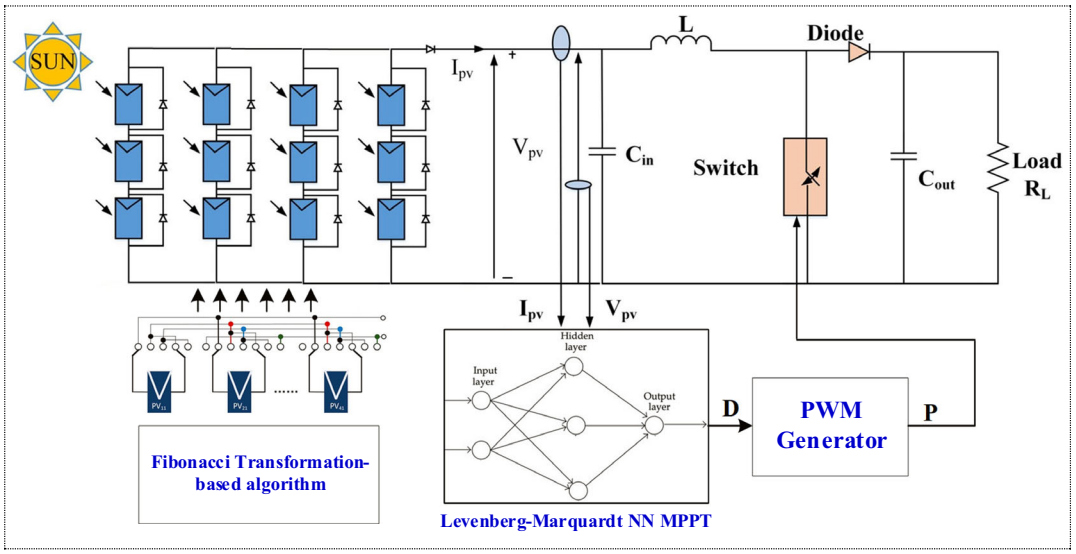

Figure 21. Levenberg–Marquardt MPPT-controlled standalone PV system with Fibonacci reconfiguration.

reconfiguration process, due to the mismatch, the arrays generate a sub-optimal power output of only 4,710.3 W, which is being effectively tracked by the LM-MPPT controller. Whereas, after the application of the reconfiguration algorithm, the mismatch variation is considerably mitigated, thus enhancing the output by 25.32%, wherein the LM-MPPT controller enables the PV array to operate at 5901.3 W, as shown in **Figure 23**. It is further noted that the tracking oscillations are about 12 W approximately, which is just 0.24% of available power.

© 2023 Wiley-VCH GmbH

21944296, 2023, 9, Downloaded from https://onlinelibrary.wiley.com/doi/10.1002/ente.202300380 by National Institute Of, Wiley Online Library on [27/11/2025]. See the Terms and Conditions (https://onlinelibrary.wiley.com/terms-and-conditions) on Wiley Online Library for rules of use; OA articles are governed by the applicable Creative Commons License

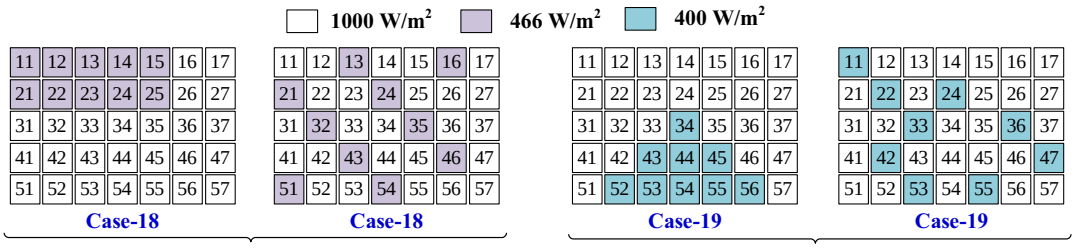

Figure 22. Shading cases (Case-18 and Case-19).

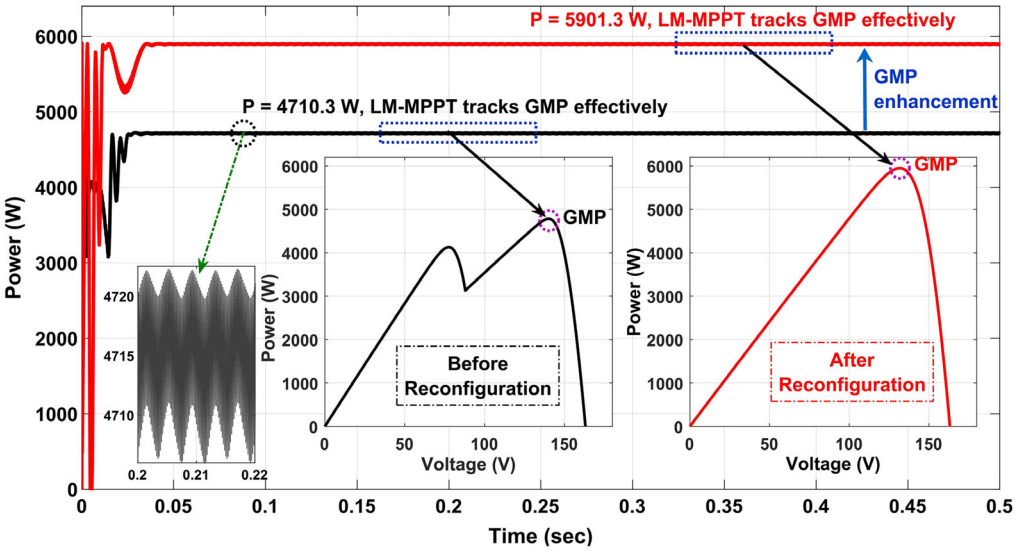

Figure 23. Output power tracked by LM-MPPT controller under Case-18.

During Case-19, a portion of the PV array is shaded where the shaded portion receives 400 W m^2. In this case, the local MPPs are much more pronounced, containing four MPPs in power–voltage curves where the GMP occurs at 4515.4 W due to a large current mismatch in rows. However, upon executing the reconfiguration approach, all these local MPPs are eliminated, and additionally, the GMP is further augmented to 5849.1 W. By employing the LM-MPPT controller, the array is operated at the augmented GMP of 5849.1 W, improving the output by 29.54%. Besides, the proposed LM-MPPT controller tracks the GMP just within 0.035 s with very fewer oscillations, as shown in **Figure 24**.

4.5. Evaluation with Wilcoxon Signed Rank Sum Test

To verify the reliability and consistency of the generated power by FT technique under various shading conditions and to demonstrate its notable variation w.r.t. existing techniques statistically, a nonparametric statistical hypothesis Wilcoxon signed rank sum test[46] with a significant difference (p-value) of 0.05 has been considered to perform a pairwise unbiased comparative assessment among the examined techniques as detailed in Table 4. The test has been conducted as follows: 1) Obtain the GMP values of various configurations under distinct PS cases. 2) Compute "R_+", the sum of positive ranks for which the proposed techniques render the highest GMP over the existing ones. 3) Compute "R_-", the sum of negative ranks for which the existing techniques deliver more GMP than the proposed techniques. 4) Calculate p-value that exhibits the notable variation of the obtained results in a statistical hypothesis testing. Lesser the p-value (<0.05), there is ample evidence against the null hypothesis suggesting a remarkable difference between the techniques.

The results reported in **Table 5** show that there exists a notable difference between FT and the existing techniques, as the p-values are less than 0.05 for 14 techniques. Further, w.r.t the remaining eight techniques, the p-values are 0.067 (which is just slightly more than 0.05), indicating that there is still a considerable difference in their performance. The computed R_+ and R_- values reveal that the proposed FT is capable enough of achieving the highest GMP than the existing ones as R_+ is far greater than R_-. Further, the proposed technique validates its supremacy in rendering an effectively consistent performance under all shading conditions for various array sizes. **Figure 25** shows the overall performance comparison of the proposed FT with the existing reconfiguration techniques.

4.6. Comparison of State-Of-The-Art Techniques with Proposed Technique

The contrast of the proposed algorithm with the contemporary state-of-the-art methods is detailed as follows: 1) The proposed

© 2023 Wiley-VCH GmbH

21944296, 2023, 9, Downloaded from https://onlinelibrary.wiley.com/doi/10.1002/ente.202300380 by National Institute Of, Wiley Online Library on [27/11/2025]. See the Terms and Conditions (https://onlinelibrary.wiley.com/terms-and-conditions) on Wiley Online Library for rules of use; OA articles are governed by the applicable Creative Commons License

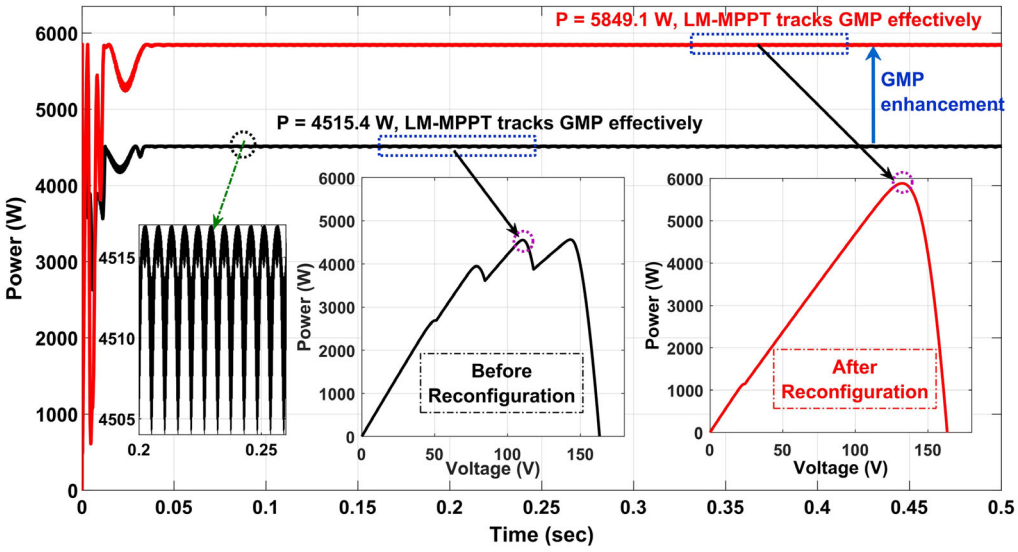

Figure 24. Output power tracked by LM-MPPT controller under Case-19.

Table 5. Nonparametric statistical hypothesis Wilcoxon signed-rank sum test of FT versus existing techniques.

FT vs	R_+	R_-	*p*-value	FT vs	R_+	R_-	*p*-value
TCT	10	0	0.067889	OSU[24]	10	0	0.067889
SD[14]	15	0	0.043114	OEA[25]	15	0	0.043114
FP[15]	15	0	0.043114	OEP[26]	15	0	0.043114
LS[17]	10	0	0.067889	NA[27]	15	0	0.043114
OSA[18]	15	0	0.043114	DT[28]	21	0	0.027707
NOS[18]	15	0	0.043114	MS[29]	15	0	0.043114
SM[19]	15	0	0.043114	CS[29]	15	0	0.043114
CI[20]	15	0	0.043114	AS[31]	15	0	0.043114
SC[21]	10	0	0.067889	CM[32]	10	0	0.067889
IS[22]	15	0	0.043114	SPA[33]	10	0	0.067889
LOS[23]	10	0	0.067889	HM[35]	10	0	0.067889

reconfiguration approach does not use switching matrices, decides on switching matrices at the best possible rate, and does not have memory-related switching matrix operation problems, in contrast to neural network-based approaches.[12,13] 2) The population-based metaheuristic algorithms[7–11] necessitate large search space, slow convergence issues, choice of parameter challenges, local optimum trapping issues, selection of weights issues, lengthy calculations and computations, requires too much time for computations, etc. The proposed methodology doesn't have any such problems. 3) The EAR-based dynamic methods[47] need a regulator to deliver the gating pulses for power switches as per the dispersed shade pattern. Besides, a massive number of switching patterns to determine the optimum array configuration. In contrast, the proposed strategy is a one-time solution and doesn't necessitate the aforementioned issues. 4) The game-puzzle-based methods[14–18,21–24,29–31] are not scalable, compatible for all array sizes, and hence their deployment is very limited, whereas the proposed algorithm can be employable for any array size. 5) The previously proposed shifting and indexing-based[19,20,28,36] techniques have several drawbacks that the proposed method successfully resolves. Some of the shortcomings include inadequate scalability, exhibiting significant diagonal correlation between panels, inconsistencies, etc. 6) Notwithstanding being extensible for any array size, the numbering-based OE and OEP[25,26] approaches offer inconsistencies in performance with a substantial correlation between successive shaded panels row-wise. The proposed method, in contrast, not only has global compatibility but also consistently performs better in low irradiation conditions. 7) The other approaches[35,36] exhibit a very high correlation between the row-wise and diagonal-wise modules leading to a significant mismatch. In difference, the proposed method considerably reduces the relation among the row-wise, column-wise, and diagonal-wise shaded panels.

5. Conclusions

An inclusive literature survey of existing reconfiguration strategies with their advantages and limitations is discussed in detail. A novel reconfiguration approach inspired by the integer sequence-based FT employing the idea of image encryption is proposed to reduce the shading losses optimally. The proposed FT overcomes the limitations of the existing ones to a greater degree, and it is validated for symmetric (9×9, 4×4) and asymmetric (4×8) PV arrays under 17 shading cases. Further, its effectiveness is compared with the 23 existing configurations. With the proposed FT configuration for 9×9, and 4×8 PV arrays, the GMP enhancement is in the range of (5.06–34.43)% and (4.35–37.39)%, respectively. The uniqueness of FT technique is its effectiveness in evenly distributing the shade by lessening the correlation between adjoining shaded panels of an array, thereby lowering the row current mismatch. This distinctive feature resulted in the highest GMP and improved characteristics with the least MPPs reducing the burden on MPPT trackers. The proposed configuration is validated experimentally for a 4×4 PV array. The proposed algorithm is further validated using

© 2023 Wiley-VCH GmbH

21944296, 2023, 9, Downloaded from https://onlinelibrary.wiley.com/doi/10.1002/ente.202300380 by National Institute Of, Wiley Online Library on [27/11/2025]. See the Terms and Conditions (https://onlinelibrary.wiley.com/terms-and-conditions) on Wiley Online Library for rules of use; OA articles are governed by the applicable Creative Commons License

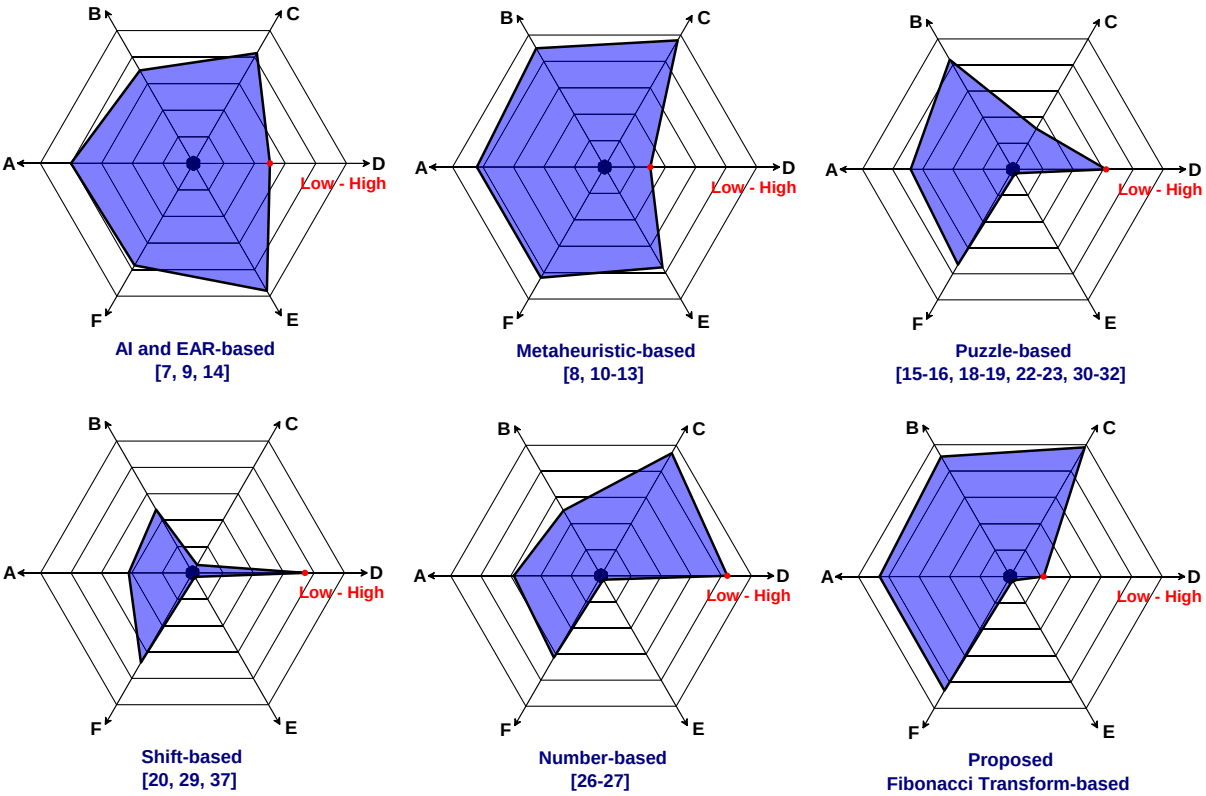

Figure 25. Overall performance comparison of the proposed technique with state-of-the-art approaches. A) GMP yield, B) Shade dispersion capability, C) Scalability, D) Exhibited MPPs, E) Sensors & switches requirement, F) Performance enhancement.

the Levenberg–Marquardt neural network-based MPPT controller for a 7 kW_p standalone PV system under distinct shading conditions. The lowest *p*-value of the Nonparametric Wilcoxon signed-rank sum test confirms the consistency and effectiveness of the proposed technique over the existing ones. It is remarked from the in-depth qualitative and quantitative analysis that the proposed integer-based reconfiguration strategy offers the optimal solution in mitigating the shading effects significantly.

6. Future Scope

The proposed approaches can be effectively utilized in the future for PV array dynamic reconfiguration procedures to determine the optimum switching matrix pattern. Further research can be done on the proposed reconfiguration method for GMP augmentation and its tracking with sophisticated MPPT trackers for rooftops and large-capacity commercial operations of PV installations.

Conflict of Interest

The authors declare no conflict of interest.

Data Availability Statement

Research data are not shared.

Keywords

Fibonacci, global maximum power, image encryption, photovoltaics, reconfiguration

Received: April 7, 2023
Revised: May 14, 2023
Published online: June 19, 2023

[1] C. A. Rao, R. D. A. Raj, K. A. Naik, *Int. J. Circuit Theory Appl.* **2023**, https://doi.org/10.1002/cta.3629.
[2] B. Babes, F. Albalawi, N. Hamouda, S. Kahla, S. S. M. Ghoneim, *IEEE Access* **2021**, *9*, 159933.
[3] R. D. A. Raj, K. A. Naik,, *Energy Sources A* **2022**, *44*, 951.
[4] N. Hamouda, B. Babes, S. Kahla, Y. Soufi, J. Petzoldt, T. Ellinger, in *1st Int. Conf. on Sustainable Renewable Energy Systems and Applications*, IEEE, Piscataway, NJ **2019**.
[5] B. Babes, A. Boutaghane, N. Hamouda, *Neural Comput. Appl.* **2022**, *34*, 299.
[6] N. Hamouda, B. Babes, S. Kahla, A. Boutaghane, A. Beddar, O. Aissa, *Int. Conf. on Electrical Engineering (ICEE)*, IEEE, Piscataway, NJ **2020**.
[7] S. N. Deshkar, S. B. Dhale, J. S. Mukherjee, T. S. Babu, N. Rajasekar, *Renew. Sustain. Energy Rev.* **2015**, *43*, 102.
[8] T. S. Babu, J. P. Ram, T. Dragičević, M. Miyatake, F. Blaabjerg, N. Rajasekar, *IEEE Trans. Sustain. Energy* **2018**, *9*, 74.
[9] D. Yousri, S. B. Thanikanti, K. Balasubramanian, A. Osama, A. Fathy, *IEEE Access* **2020**, *8*, 159931.
[10] A. M. Ajmal, V. K. Ramachandaramurthy, A. Naderipour, J. B. Ekanayake, *Energy Convers. Manage.* **2021**, *230*, 113806.

© 2023 Wiley-VCH GmbH

21944296, 2023, 9, Downloaded from https://onlinelibrary.wiley.com/doi/10.1002/ente.202300380 by National Institute Of, Wiley Online Library on [27/11/2025]. See the Terms and Conditions (https://onlinelibrary.wiley.com/terms-and-conditions) on Wiley Online Library for rules of use; OA articles are governed by the applicable Creative Commons License

[11] D. Yousri, T. S. Babu, S. Mirjalili, N. Rajasekar, M. A. Elaziz, *Energy Convers. Manage.* **2020**, *225*, 113385.
[12] M. Karakose, M. Baygin, K. S. Parlak, in *Int. Conf. on Renewable Energy Research and Application* **2014**, pp. 633–637.
[13] M. Karakose, M. Baygin, K. Murat, N. Baygin, E. Akin, *Intl. J. Comput. Intell. Syst.* *9*, 202.
[14] B. I. Rani, G. S. Ilango, C. Nagamani, *IEEE Trans. Sustain. Energy* **2013**, *4*, 594.
[15] H. S. Sahu, S. K. Nayak, S. Mishra, *IEEE J. Emerg. Select. Topics Power Electron.* **2016**, *4*, 626.
[16] N. Rakesh, T. V. Madhavaram, *Front. Energy* **2016**, *10*, 227.
[17] R. Pachauri, A. S. Yadav, Y. K. Chauhan, A. Sharma, V. Kumar, *Int. Trans. Electr. Energy Syst.* **2018**, *28*, 2556.
[18] M. Horoufiany, R. Ghandehari, *Sol. Energy* **2018**, *159*, 1037.
[19] N. Belhaouas, M.-S. Ait Cheikh, P. Agathoklis, M.-R. Oularbi, B. Amrouche, K. Sedraoui, N. Djilali, *Appl. Energy* **2017**, *187*, 326.
[20] S. Pillai, J. P. Ram, M. S. S. Nihanth, N. Rajasekar, *Energy Convers. Manage.* **2018**, *172,* 402.
[21] M. S. S. Nihanth, J. P. Ram, D. S. Pillai, A. M. Y. M. Ghias, A. Garg,, *Sol. Energy* **2019**, *194*, 209.
[22] S. Krishna, T. Moger, *Renew. Sust. Energ. Rev.* **2019**, *109*, 333.
[23] R. Venkateswari, N. Rajasekar, *Energy Convers. Manage.* **2020**, *215*.
[24] S. G. Krishna, T. Moger, *IEEE Trans. Energy Convers.* **2019**, *34*, 1973.
[25] K. Yadav, B. Kumar, D. Swaroop, *Energy Rep.* **2020**, *6*, 427.
[26] S. S. Reddy, C. Yammani, *Energy* **2020**.
[27] M. S. S. Nihanth, N. Rajasekar, D. S. Pillai, J. P. Ram, *Lect. Notes Electr. Eng.* **2020**, *607*.
[28] V. P. Madhanmohan, M. Nandakumar, A. Saleem, *Energy Sources A Recov. Utiliz. Environ. Effects* **2020**.
[29] S. Anjum, V. Mukherjee, G. Mehta, *ASME J. Sol. Energy Eng.* **2021**, *143*, 061003.
[30] C. Ye, C. Tai, Y. Huang, J. Chen, *Energy Conv. Manage.* **2021**, *246*, 114675.
[31] G. Bharti, V. M. R. Tatabhatla, T. Kanumuri, in *Proc. of the Int. Conf. on Paradigms of Computing, Communication and Data Sciences*, Vol. *15*, **2021**.
[32] V. M. R. Tatabhatla, A. Agarwal, T. Kanumuri, *IEEE Trans. Energy Convers.* **2022**, *37*, 811.
[33] S. K. Cherukuri, P. K. Balachandran, K. R. Kaniganti, M. K. Buddi, D. Butti, S. Devakirubakaran, T. S. Babu, H. H. Alhelou,, *IEEE Access* **2021**, *9*, 123103.
[34] S. Mikkili, A. Kanjune, P. K. Bonthagorla, T. Senjyu, *Energies* **2022**, *156*, 2124.
[35] R. D. A. Raj, K. A. Naik, *IETE J. Res.* **2022**, 1.
[36] V. R. Krishnan, F. Blaabjerg, A. Sangwongwanich, *IEEE J. Photovolt.* **2022**, *12*, 871.
[37] R. D. Amar Raj, K. A. Naik, *Int. J. Circuit Theory Appl.* **2022**, *51*, 668.
[38] K. A. Naik, R. D. A. Raj, C. V. Rao, T. S. Babu, *Energy Convers. Manage.* **2022**, *272*, 116376.
[39] A. Raj, R. David, K. A. Naik, *J. Sol. Energy Eng.* **2022**, *144*, 061001.
[40] A. K. Supriatna, E. Carnia, M. Z. Ndii, *Heliyon* **2019**, *5*, 01130.
[41] M. Mishra, P. Mishra, M. C. Adhikary, S. Kumar, *Int. J. Cryptograph. Inform. Secur.* **2012**, *2*, 131.
[42] R. D. A. Raj, K. A. Naik,, *Energy Conv. Manage.* **2022**, *261*, 115666.
[43] R. K. Koppanati, K. Kumar, *IEEE Consumer Electron. Mag.* **2021**, *10*, 41.
[44] B. M. Ozyildirim, M. Kiran, *Neural Netw.* **2021**, *143*, 564.
[45] B. Babes, A. Boutaghane, N. Hamouda, S. Kahla, A. Kellai, T. Ellinger, J. Petzoldt, *J. Eur. Syst. Autom.* **2020**, *53*, 811.
[46] W. Hernandez, J. L. Maldonado-Correa, *IEEE Trans. Energy Convers.* **2017**, *32*, 394.
[47] G. H. K. Varma, V. R. Barry, R. K. Jain, *IEEE Access* **2022**, *10*, 4832.

© 2023 Wiley-VCH GmbH

21944296, 2023, 9, Downloaded from https://onlinelibrary.wiley.com/doi/10.1002/ente.202300380 by National Institute Of, Wiley Online Library on [27/11/2025]. See the Terms and Conditions (https://onlinelibrary.wiley.com/terms-and-conditions) on Wiley Online Library for rules of use; OA articles are governed by the applicable Creative Commons License